Three-dimensional instabilities over a rectangular open cavity: from linear stability analysis to experimentation

J. de Vicente[1],†, **J. Basley**[2,3,4], **F. Meseguer-Garrido**[1], **J. Soria**[2] and **V. Theofilis**[1]

[1]School of Aerospace Engineering, Universidad Politécnica de Madrid, Pza. Cardenal Cisneros 3, E-28040 Madrid, Spain

[2]Laboratory for Turbulence Research in Aerospace and Combustion, Department of Mechanical and Aerospace Engineering, Monash University, Clayton 3800, Australia

[3]CNRS, Laboratoire d'Informatique pour la Mécanique et les Sciences de l'Ingénieur, F-91403 Orsay, France

[4]Université Paris-Sud, F-91405 Orsay, France

Three-dimensional instabilities arising in open cavity flows are responsible for complex broad-banded dynamics. Existing studies either focus on theoretical properties of ideal simplified flows or observe the final state of experimental flows. This paper aims to establish a connection between the onset of the centrifugal instabilities and their final expression within the fully saturated flow. To that end, a linear three-dimensional modal instability analysis of steady two-dimensional states developing in an open cavity of aspect ratio $L/D = 2$ (length over depth) is conducted. This analysis is performed together with an experimental study in the same geometry adding spanwise endwalls. Two different Reynolds numbers are investigated through spectral analyses and modal decomposition. The physics of the flow is thoroughly described exploiting the strengths of each methodology. The main flow structures are identified and salient space and time scales are characterised. Results indicate that the structures obtained from linear analysis are mainly consistent with the fully saturated experimental flow. The analysis also brings to light the selection and alteration of certain wave properties, which could be caused by nonlinearities or the change of spanwise boundary conditions.

Key words: instability, cavity flow

1. Introduction

Flow over open cavities is of theoretical and practical interest from both a hydrodynamic and an aeroacoustic point of view. Two-dimensional cavities, i.e. those in which flow in the lateral spatial direction is considered to be homogeneous, may be encountered in planar or axisymmetric form, embedded in incompressible

† Email address for correspondence: fj.devicente@upm.es

or compressible flow over semi-infinite (open) or confined (closed) domains. Geometric details of an open cavity configuration, such as its cross-sectional shape, length-to-depth aspect ratio and the form of either or both cavity lips, as well as the relative dimension of the cavity compared with a characteristic length scale of the oncoming flow, make description of open cavity flow non-unique. A finite spanwise extent of the cavity, i.e. three-dimensionality of the cavity geometry itself, adds yet another dimension to this multi-parametric problem, as does turbulence, the latter being essential for the description of most industrially relevant flows.

From a theoretical point of view, progress in the understanding of the complex open cavity flow dynamics is made by addressing the relatively simple two-dimensional rectangular cavity configuration at moderate Reynolds numbers. In this context, a steady laminar two-dimensional boundary layer on a flat surface encountering an open cavity separates as a free shear layer from the upstream cavity corner. Two independent Reynolds numbers characterise this flow, one based on the incoming boundary-layer flow properties and a second based on the cavity dimensions. At the relatively low Reynolds number values of interest here, at which two-dimensional flow remains laminar, and depending on the cavity aspect ratio, the free shear layer either impinges upon the downstream cavity corner in a steady or unsteady manner, or curves toward the cavity floor to form a closed recirculation bubble. In either case, a new boundary layer forms on the downstream cavity wall, starting from the downstream cavity corner, which may itself be steady or unsteady.

The study of the stability of flow over open cavities has been historically focused on the self-sustained oscillations of the shear layer (Powell 1953; Rockwell 1977; Rockwell & Naudascher 1979). These instabilities along the mouth of the cavity are enhanced through a feedback mechanism initiated by vortex–edge interactions at the downstream corner of the cavity. This feedback is acoustic in nature for it relies on the pressure disturbances radiating from the impingement and forcing the vortex shedding at separation. The resulting locked-on modes of oscillation involve frequencies that satisfy the Rossiter (1964) semi-empirical formula, established for compressible flows. In the incompressible regime, the pressure feedback is also active and can be considered as instantaneous. The self-sustained oscillations follow the primarily two-dimensional geometry of the shear layer. However, the experimental study of shear-layer instabilities reported three-dimensional structures in the flow with frequencies far smaller than the ones of the Rossiter modes (Rockwell & Knisely 1980; Koseff & Street 1984*b*; Neary & Stephanoff 1987). Cattafesta III *et al.* (1998) and Kegerise *et al.* (2004) concluded that these low-frequency oscillations were not the result of nonlinear interaction between Rossiter modes.

The first full three-dimensional global instability analysis of compressible flow over a rectangular open cavity was performed by Brès & Colonius (2008). In that work the authors establish that the low-frequency mode corresponds to three-dimensional structures associated with the main recirculation vortex inside the cavity. More recently, the studies by Faure *et al.* (2009) characterised experimentally the three-dimensional structures in the open cavity and confirm that the dynamical structures are independent of shear-layer instabilities.

It is interesting to note that such spanwise dynamics arise in the recirculating flow in shear-driven as well as lid-driven cavities (Theofilis 2000; Albensoeder, Kuhlmann & Rath 2001; de Vicente *et al.* 2010; Gonzalez *et al.* 2011), that is, regardless of the shear-layer oscillations.

The present work aims to bring more insights into the early stages of the three-dimensional dynamics associated with centrifugal effects around the main

recirculation inside the cavity, in a flow regime in which the shear-layer modes are not dominant. The unstable three-dimensional perturbations are identified and characterised from both numerical and experimental approaches. Moreover, the fruitful combination of linear analysis and experiments leads to a deeper knowledge of the characteristics and evolution of these modes from their onset to their final presence in the nonlinear saturated state.

Section 2 describes the numerical methodology used in the resolution of the stability analysis of open cavity flows with respect to spanwise-periodic three-dimensional instabilities. Using the terminology proposed by Theofilis, Colonius & Seifert (2001), BiGlobal analysis has been applied to the two-dimensional basic state to recover the three-dimensional perturbations. The configuration investigated by Brès & Colonius (2008) is used here as a reference and revisited in the incompressible limit. A comprehensive overview of the critical values for the multi-parametric flow problem in hand is given for the first time, to the best of the authors' knowledge, and the nature of the leading eigenmodes is discussed.

In § 3, the experimental set-up and the post-processing of the experimental data are described. Two particular flow regimes are investigated and analysed through the space–time dynamics of the spanwise fluctuations within the inner flow in its saturated state. In particular, space-extended Fourier modes are identified, as well as the characteristic scales of the spanwise waves.

Results from both linear stability analysis and experiments enable the onset of centrifugal instabilities inside the cavity to be related to the final saturated state of the flow. To that end, § 4 discusses the relationship between global Fourier modes from the experiments and global eigenmodes. Section 5 summarizes the most significant conclusions obtained.

2. Linear stability analysis of the incompressible open cavity

Linear stability theory is concerned with the evolution of small-amplitude disturbances superimposed upon a laminar steady or time-periodic basic state. A modal point of view is followed and BiGlobal instability analysis has been used to analyse the flow over an open cavity of length-to-depth aspect ratio fixed at $L/D = 2$.

Lengths have been scaled with the depth of the cavity, D, and two independent Reynolds numbers are used to characterise the flow: one based on the cavity depth, $Re_D = u_\infty D/\nu$, and the other based on the boundary-layer momentum thickness (θ_0) at the upstream cavity lip (see figure 1), $Re_{\theta_0} = u_\infty \theta_0/\nu$ (where u_∞ is the streamwise velocity outside the boundary layer, and ν is the kinematic viscosity). In the incompressible flow considered, the effect on three-dimensional global flow instability of varying the parameters $(\beta, Re_D, Re_{\theta_0})$ has been analysed.

Most of the linear analysis results presented in this work have been obtained fixing the displacement thickness of the boundary layer at the inflow boundary, x_{-1}, to $\delta_{-1}^* = 0.25$ (corresponding to momentum thickness $\theta_{-1} = 0.0337$), and also, keeping constant the distance between the inflow boundary and the upstream cavity lip, $x_0 - x_{-1} = D$. The reason for this procedure is to reduce the degrees of freedom in the comparison with experimental work and other authors' numerical results. Results documenting eigenmode dependence on the incoming boundary-layer thickness are shown at the end of this section. The full parametric study, including the effect of cavity length-to-depth aspect ratio, L/D, is presented by Meseguer-Garrido *et al.* (2011).

2.1. *Base flow calculations*

The steady two-dimensional base flow, required in the BiGlobal analysis, is obtained by direct numerical simulation (DNS), using a semi-implicit artificial compressibility
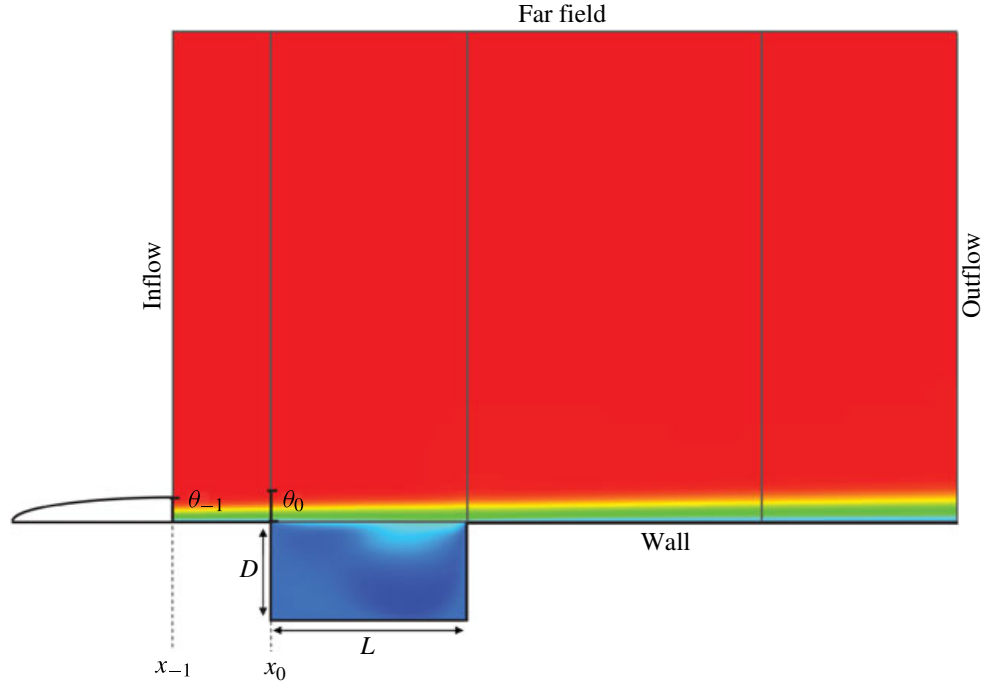
FIGURE 1. (Colour online) Schematic description of the two-dimensional open cavity and problem parameters.

method detailed in de Vicente *et al.* (2010). A spectral collocation multi-domain methodology based on Chebyshev polynomials presented there is employed, making use of the natural decomposition of the cavity into rectangular subdomains, as schematically depicted in figure 1. In that figure, in addition to the main geometrical parameters involved in the analysis, the streamwise velocity is plotted at conditions $Re_D = 1500$ and $Re_{\theta_0} = 56.81$.

Regarding the boundary conditions utilised, on the solid walls the viscous conditions discussed by de Vicente *et al.* (2010) have been applied. At the inflow boundary a Blasius profile is imposed, corresponding with the appropriate Reynolds number and incoming boundary-layer thickness, while the outflow, x_∞, and far field, y_∞, boundaries have been placed at large distances from the cavity in order to minimise numerical effects due to the imposition of artificial boundary conditions for open flows (de Vicente *et al.* 2011). Typical parameters chosen are $y_\infty = 5$ and $x_\infty = 8$. Table 1 summarises the steady flow results obtained at different Reynolds numbers; those at $Re_D = 1500$ correspond to run '2M01' in the work of reference by Brès & Colonius (2008) and will be discussed further in what follows. Both $Re_D = 1500$ and $Re_D = 2400$ cases will be analysed in depth from a numerical and experimental point of view in §4.

2.2. *Global instability analysis*

A modal linear instability analysis framework is utilised in the present work. The three-dimensional space is taken to comprise an inhomogeneous two-dimensional domain on which the cavity is defined. This is extended periodically in z and characterised by a wavelength L_z, related to a real spanwise wavenumber $\beta = 2\pi/L_z$. The decomposition of the flow $\boldsymbol{q}$

$$\boldsymbol{q}(x, y, z, t) = \bar{\boldsymbol{q}}(x, y) + \epsilon \hat{\boldsymbol{q}}(x, y) \exp\{\mathrm{i}(\beta z - \omega t)\} \tag{2.1}$$

Re_D	x_0	δ_0^*	θ_0	Re_{θ_0}	(x_C, y_C)	(x_c, y_c)
1100	3.845	0.1017	0.0392	43.19	$(1.408, -0.412)$	$(1.381, -0.594)$
1300	4.363	0.0996	0.0384	50.01	$(1.409, -0.417)$	$(1.388, -0.566)$
1500	4.880	0.0981	0.0378	56.81	$(1.410, -0.420)$	$(1.393, -0.536)$
1700	5.397	0.0969	0.0374	63.61	$(1.412, -0.422)$	$(1.397, -0.515)$
1900	5.915	0.0960	0.0370	70.39	$(1.414, -0.425)$	$(1.398, -0.498)$
2400	7.207	0.0943	0.0363	87.33	$(1.418, -0.429)$	$(1.400, -0.473)$

TABLE 1. Parameters characterising the inflow Blasius boundary layer and associated location of the primary, (x_C, y_C), and secondary, (x_c, y_c), vortices.

is introduced into the incompressible fluid flow equations, followed by a linearisation about the base state $\bar{q}$. The flow state is defined by the velocity components in each direction (u, v, w) and the pressure (P). An important simplification comes from the absence of the z-component in the velocity profile of the base flow $\bar{w} = 0$. Homogeneity in the spanwise direction (β real) and the redefinitions

$$i\bar{w} \rightarrow \bar{w}, \quad i\omega \rightarrow \omega \qquad (2.2a,b)$$

result in the following generalized real non-symmetric eigenvalue problem:

$$\left[\mathcal{L}_2 - (\mathcal{D}_x\bar{u})\right]\hat{u} - \left(\mathcal{D}_y\bar{u}\right)\hat{v} - \mathcal{D}_x\hat{P} = \omega\hat{u}, \qquad (2.3)$$

$$-\left(\mathcal{D}_x\bar{v}\right)\hat{u} + \left[\mathcal{L}_2 - \left(\mathcal{D}_y\bar{v}\right)\right]\hat{v} - \mathcal{D}_y\hat{P} = \omega\hat{v}, \qquad (2.4)$$

$$\mathcal{L}_2\bar{w} - \beta\hat{P} = \omega\bar{w}, \qquad (2.5)$$

$$\mathcal{D}_x\hat{u} + \mathcal{D}_y\hat{v} - \beta\bar{w} = 0, \qquad (2.6)$$

where

$$\mathcal{L}_2 = \frac{1}{Re}\left(\frac{\partial^2}{\partial x^2} + \frac{\partial^2}{\partial y^2} - \beta^2\right) - \bar{u}\frac{\partial}{\partial x} - \bar{v}\frac{\partial}{\partial y}, \qquad (2.7)$$

or, in schematic form,

$$\boldsymbol{A}\hat{\boldsymbol{q}} = \omega\boldsymbol{B}\hat{\boldsymbol{q}}. \qquad (2.8)$$

The complex eigenvalue ω has two components, the amplification/damping rate ω_r, and the frequency ω_i. This allows to define the dimensionless Strouhal number based on cavity depth as $St_D = \omega_i D/(2\pi u_\infty)$ Solutions of (2.8) are sought subject to the following boundary conditions for the disturbance quantities. At solid walls the no-slip boundary condition is imposed on the velocity components, alongside a compatibility condition for the disturbance pressure. The imposition of appropriate boundary condition for open boundaries is not straightforward. Homogeneous Dirichlet boundary conditions at the inflow and far field are imposed on the perturbation velocity components, while a homogeneous Neumann boundary condition in the normal direction is considered for the disturbance pressure. At the outflow boundary Neumann conditions are applied on all the perturbation variables,

$$\frac{\partial\hat{u}}{\partial n} = \frac{\partial\hat{v}}{\partial n} = \frac{\partial\bar{w}}{\partial n} = \frac{\partial\hat{P}}{\partial n} = 0. \qquad (2.9)$$

This choice has been proven to be appropriate for the leading cavity mode, whose structure is confined within the cavity.
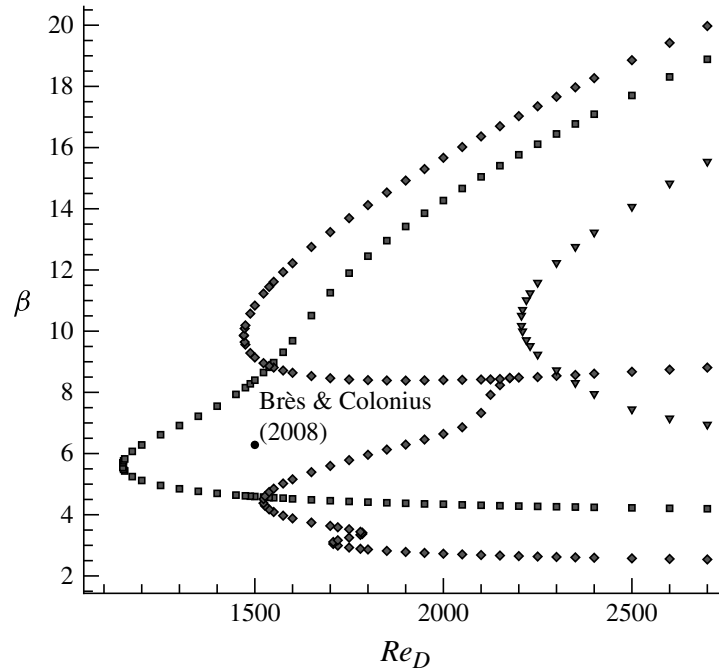
FIGURE 2. Neutral stability curves of the three leading modes in the open cavity flow of aspect ratio $L/D = 2$ with $\theta_{-1} = 0.0337$. Squares show Mode I, diamonds Mode II and inverted triangles Mode III. Neutral values are listed in table 2.

2.3. *Global instability results*

Extensive validation of the instability analysis algorithm has been performed. Previous works (de Vicente 2010; de Vicente *et al.* 2010) have validated the domain decomposition methodology and the accuracy of the resulting solution.

The most significant result obtained using the BiGlobal analysis is the identification of the critical parameters related to the destabilisation of the flow over the open cavity. To illustrate this behaviour is useful to map the different regions in the parametric space depending on the nature of the flow. The neutral curves corresponding to the first three cavity eigenmodes are presented in figure 2. These curves are obtained as a sequence of the neutral points extracted using a systematic scan of the relevant Reynolds number and wavenumber ranges. The value of the momentum thickness of the incoming boundary layer at the inflow of the computational domain is fixed at $\theta_{-1} = 0.0337$. Hence, in the upstream lip of the cavity Re_{θ_0} varies from $Re_{\theta_0} = 43.19$ to 87.33 when Re_D increases from the very stable $Re_D = 1100$ to the unstable $Re_D = 2900$. The fine parametric scan employed ($\Delta Re_D \simeq 1$, $\Delta\beta \simeq 0.01$ in the nose of the modes) permits a precise identification of the three-dimensional critical conditions for global instability analysis, which are presented in table 2.

Figure 2 provides additional interesting information related to the global stability of the cavity flow. It can be stated that below $Re_D = 1149$ the basic flow is three-dimensional globally stable. As Re_D increases, unstable perturbations, initially confined inside the cavity, begin to appear. The characteristics of these leading eigenmodes, I, II and III in table 2, are explained in what follows.

Regarding the behaviour of these modes, Mode I, the first to become unstable (see figure 3) is associated with a pair of complex-conjugate eigenvalues, commonly referred in the literature as a travelling mode ($\omega_i \neq 0$). In the range of Reynolds number $Re_D \simeq [1149, 1650]$ this disturbance has the highest amplification rate, but for Reynolds numbers higher than $Re_D \simeq 1650$, the second mode becomes dominant.

Mode	Re_{crit}	β_{crit}	St_D
I	1149	5.62	0.027
II(a)	1471	9.86	0.0000
II(b)	1522	4.45	0.010
III	2207	10.34	0.054

TABLE 2. Critical parameters of the first three modes for the open cavity flow with aspect ratio $L/D = 2$ and $\theta_{-1} = 0.0337$.
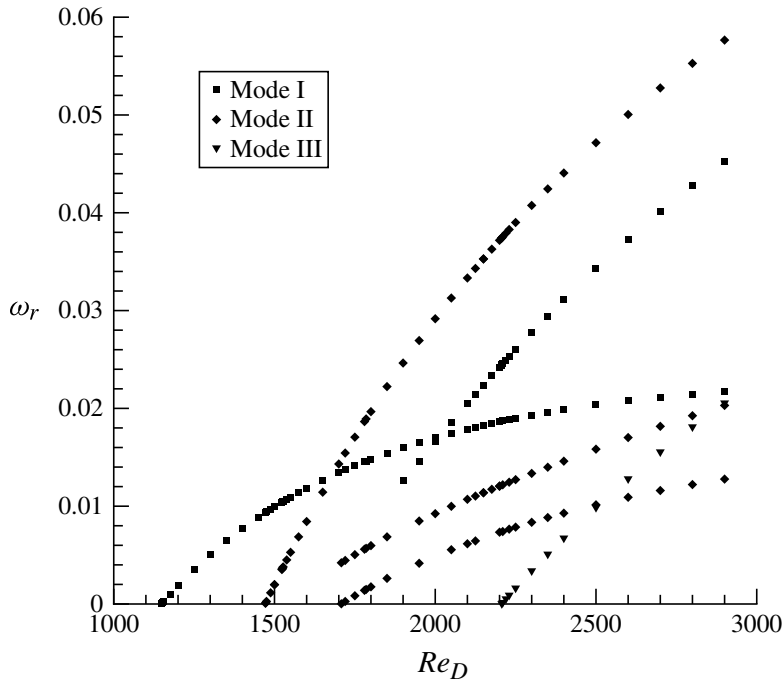

FIGURE 3. Dependence on Reynolds number of the amplification rate, ω_r, of the leading eigenmodes.

This second mode consists of two different branches. The first one, referred to as Mode II(a), is a stationary mode ($St_D = 0$) present for high wavenumbers, ($\beta > 8.5$), and it is three-dimensionally stable for Reynolds numbers lower than $Re_D = 1471$. The second branch of this mode becomes unstable at $Re_D = 1522$, and, like Mode I, is a travelling disturbance composed by two complex conjugate eigenvalues (Mode II(b) in table 2). This pair of eigenvalues splits above $\beta \simeq 8.5$ into two stationary branches, one of which becomes stabilised, and bears no relevance in this analysis, while the other one becomes less stable further from the junction in the parameter space. This unstable stationary branch of Mode II is the one that becomes dominant with increasing Reynolds numbers, as can be seen in figure 3. The third eigenmode to become unstable (Mode III in table 2) is also a travelling disturbance.

The amplitude functions of the leading eigenmode corresponding to the critical parameters $Re_D = 1149$ and $\beta = 5.62$ are depicted in figure 4. As can be observed, instability activity is confined within the cavity, where all the amplitude functions reach their respective maxima, while the disturbance flow field outside the cavity remains benign.

The last effect to be analysed is the response of the two leading modes to the variation of the incoming boundary-layer momentum thickness. To perform this study
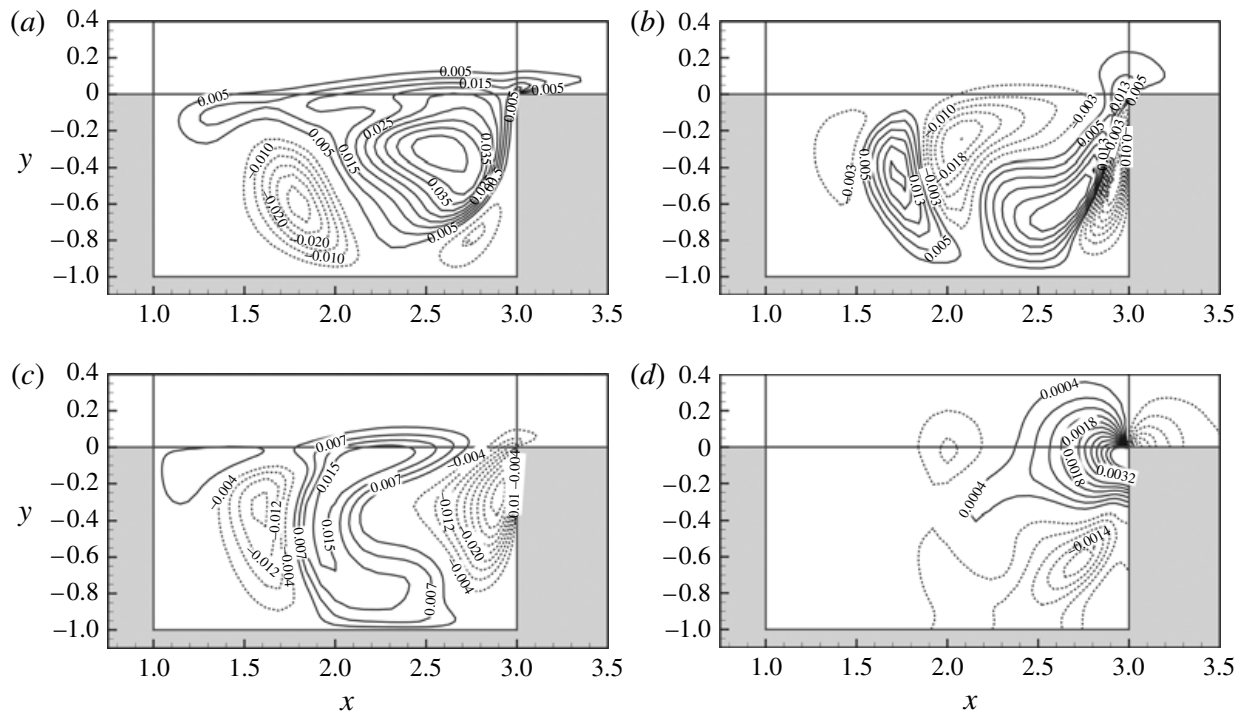
FIGURE 4. Close-up view of the spatial structure of the amplitude functions of the most unstable eigenmode $\omega = (0.000\,11, \pm 0.172\,08)$ at critical $Re_D = 1149$ and $\beta = 5.62$. (a) $\hat{u}(x, y)$; (b) $\hat{v}(x, y)$; (c) $\bar{w}(x, y)$; (d) $\hat{P}(x, y)$. Solid and dashed contours represent positive and negative values, respectively.
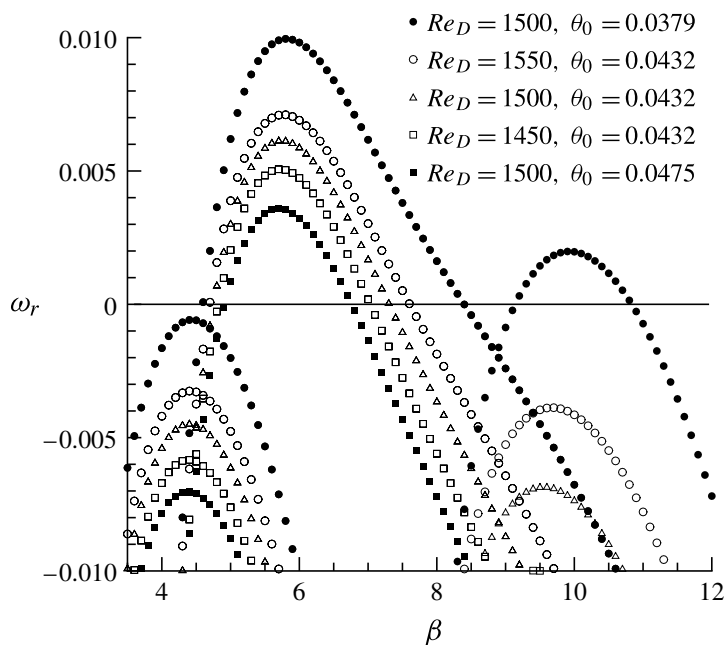

FIGURE 5. Effect of the incoming boundary-layer thickness on the flow stability.

the critical parameters Re_D and β of these modes have been tracked with the change of θ_0. The critical wavenumber β remains almost constant ($\beta = 5.62$ for the leading mode and $\beta = 9.86$ for the stationary mode) independently of the boundary-layer thickness; this effect is the same when the flow parameter modified is Re_D.

	$\tilde{\delta}_0^*$ (mm)	$\tilde{\theta}_0$ (mm)	$\theta_0 = \tilde{\theta}_0/D$	Re_{θ_0}
Linear stability analysis	4.42–8.87	1.71–3.43	0.0341–0.0685	51.2–102.9
Brès & Colonius (2008)	4.90	1.89	0.0378	56.8
Experimental data	5.59	2.16	0.0432	65.0

TABLE 3. Parameters for case A ($Re_D = 1500$).

Figure 5 shows the amplification rates of the leading modes in the critical range of β for different Re_D and θ_0 in order to quantify the effect of varying each parameter independently. Filled symbols have been obtained keeping Re_D constant ($Re_D = 1500$) while θ_0 varies from $\theta_0 = 0.0379$ to $\theta_0 = 0.0475$. Empty symbols, on the other hand, describe the change in the amplification when Re_D changes and θ_0 is fixed. As expected, increasing the boundary-layer thickness delays the three dimensional destabilisation of the flow. Being able to measure the sensitivity in the response to these two parameters is useful when comparing numerical solutions with experiments. The reference value: $Re_D = 1500$ and $\theta_0 = 0.0432$ (triangles) corresponds to the nominal parameters of the first experimental case described in what follows. Filled circles, on the other hand, correspond to the numerical computations at $Re_D = 1500$ and $\theta_0 = 0.0379$. An important remark must be made at this point: the second mode to become unstable shows a strong dependence on the aforementioned flow parameters; this effect, in addition to the rather wide margin of uncertainty in the experimental flow conditions, could affect the comparison between the two approaches, numerical and experimental.

2.4. *Discussion on numerical results*

The aim of this section is to compare, as well as contrast, the present results with previous studies of rectangular cavity flows and with additional DNS computations in order to check the validity of the BiGlobal linear analysis. The first case under consideration is Case A: $Re_D = 1500$, whose details are provided in table 3 for every methodology employed. The experimental data correspond to the nominal values for this case. Table 4 provides the associated uncertainties in these quantities.

The parametric space in the BiGlobal analysis of this case has been defined in a wide range (see table 3), to both comprise the experimental conditions and also to determine the critical instability parameters. As has been already stated, a small variation in Re_D was considered to deal with the uncertainty in the experimental flow conditions (figure 5). Through BiGlobal linear stability analysis the value of the boundary-layer momentum thickness below which the basic flow remains stable was identified. This critical value for the nominal $Re_D = 1500$ is $\theta_0 = 0.054$ corresponding to $Re_{\theta_0} = 81.44$. The characteristic wavenumber in the spanwise direction of the leading eigenmode is $\beta = 5.62$, while its temporal frequency is $St_D = 0.021$.

The constant value of θ_{-1} chosen allows a straightforward connection with the results provided by Brès & Colonius (2008). That work is to-date the most complete account of compressible flow instability over open cavities. For run 2M01 the authors detail the stability characteristics of compressible flow for an open cavity with aspect ratio $L/D = 2$ with Mach number $M = 0.1$, $Re_D = 1500$ and $Re_{\theta_0} = 56.81$. The low Mach number permits the comparison with the incompressible limit performed here. The (single) most unstable mode obtained by Brès & Colonius lies inside the
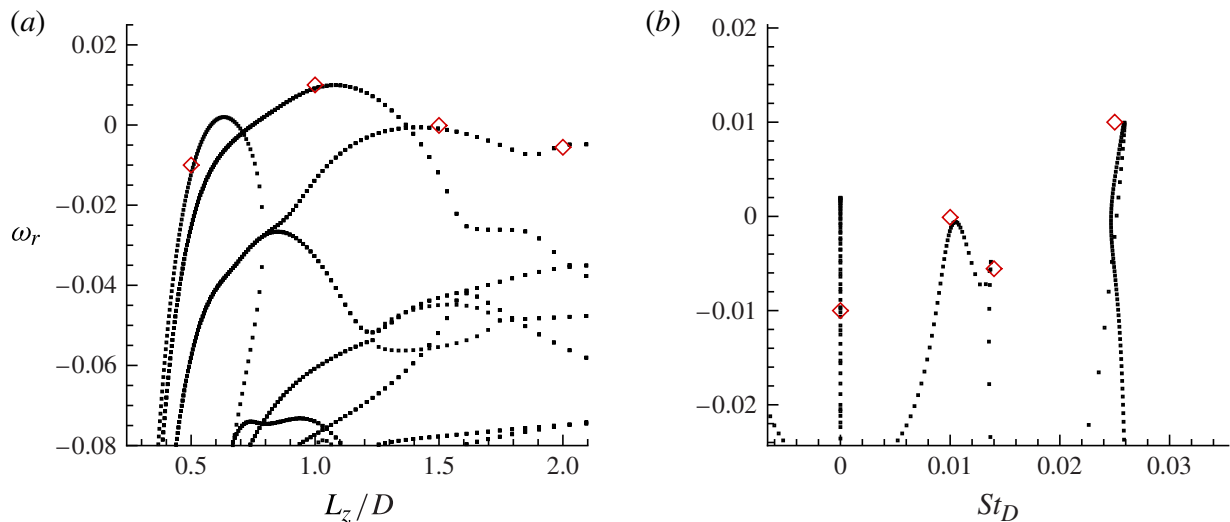
FIGURE 6. (Colour online) Comparison between the results of Brès & Colonius (2008) (open diamonds) and present BiGlobal analysis solution (black dots). (*a*) Amplification rate; (*b*) frequency of the leading disturbances as a function of the spanwise wavelength at $Re_D = 1500$.

unstable region, almost along the line of maximal amplification predicted by the present analysis.

As can be seen in figure 6 the four points provided in that work, corresponding to the three leading modes, match quite well both in frequency and amplification with the results here presented. The authors identified three different modes as the most unstable or least stable for different ranges of β, one of them being indeed unstable. The results obtained in the present work, using a finer discretization on the β parameter, show that, for the chosen flow parameters, there is another unstable mode, this one stationary, for $\beta \simeq 10$. The mode can be identified in figure 6(*a*) where a peak in the unstable region appears at $L_z \simeq 0.62$. Its stationary nature is certified in figure 6(*b*) where the peak arises when $\omega_i = 0$. It is also important to address the fact that two of the modes identified by Brès & Colonius correspond with the stationary and travelling parts of the bifurcated mode, as previously explained.

The Strouhal number corresponding to the dominant oscillation frequency, in run 2M01, is $St_D = 0.025$. The spanwise wavelength of the leading eigenmode is also reported and its value is $\beta/2\pi D = 1$. In the present analysis, the amplification rate of the leading eigenmode predicted is $\omega_r = 0.009\,81$ while the frequency is $\omega_i = 0.1623$, leading to a Strouhal number of $St_D = 0.0259$.

Isosurfaces of the spanwise velocity component ($\bar{w}$) are shown in figure 7. The three-dimensional spanwise disturbance is reconstructed periodically relating to the characteristic wavenumber $\beta = 6$, showing two wavelengths in the domain $L_z = 2.1$. These structures are in good agreement with those obtained in previous analyses, not only that of Brès & Colonius (2008) but also the earlier analysis of Theofilis & Colonius (2004) (in which only the domain inside the cavity was analysed) and that of Theofilis & Colonius (2003), who employed the residuals algorithm from Theofilis (2000), all such results presumably being related to the wake mode instability.

The second case, Case *B*: $Re_D = 2400$, exhibits a more challenging behaviour. The first drawback to consider comes from the fact that the base flow employed in the computations is artificially stabilised due to the nature of the numerical method used. The effects of using this kind of mean flow in the stability analysis have been
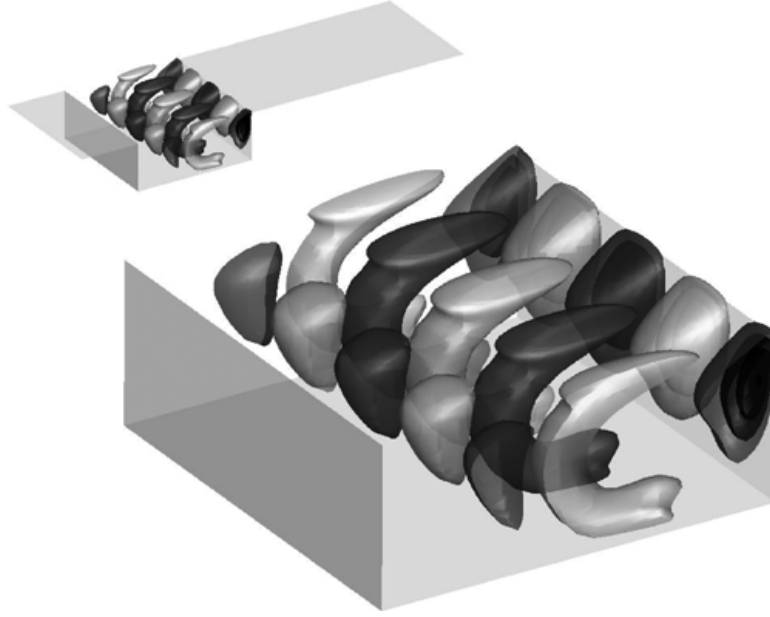
FIGURE 7. Three-dimensional visualisation of spanwise velocity at $Re_D = 1500$ and $\beta = 6$: leading disturbance obtained using BiGlobal analysis. Dark and light shadings represent positive and negative iso-values, respectively.

previously studied in Barkley (2006) for wake flows and in Piot *et al.* (2006), where a good agreement between the simulations and linear stability analysis results was observed.

BiGlobal results confirm those findings, two unstable two-dimensional perturbations being recovered: a mode with frequency $St_D \simeq 0.257$ and another with frequency $St_D \simeq 0.42$. However, in the parametric space studied, the flow exhibits three-dimensional disturbances with higher amplification rates, more relevant in the framework of this work.

According to linear analysis results, in the range $2 \lesssim \beta \lesssim 18$ the predicted numerical solution is a combination of three unstable modes. The most unstable one, see figure 3, is one of the stationary ($St_D = 0$) branches in which Mode II splits. The amplification rate of this disturbance reaches its maximum $\omega_r = 0.044$ for $\beta \simeq 11.7$.

Figure 8 depicts the isosurfaces of the three-dimensional reconstruction of the spanwise velocity component ($\bar{w}$) of the leading growing disturbance obtained by linear analysis. Two wavelengths are shown in the domain $L_z = 1.05$.

3. The experimental campaign

The experiments have been conducted in a recirculating water tunnel at the Laboratory for Turbulence Research for Aerospace and Combustion (LTRAC), Monash University. The test section is 5 m long of cross-section 500×500 mm^2 and turbulence intensity in the core region is less than 0.35 %, as shown in Parker, von Ellenrieder & Soria (2007). The experimental campaign is briefly described in the next section but the reader may refer to Basley (2012) for more details.

3.1. *Particle image velocimetry dataset*

The experimental set-up is sketched in figure 9. The test plate is mounted vertically in the middle of the test section. The 50 mm deep, *D*, 100 mm long, *L*, cavity spans
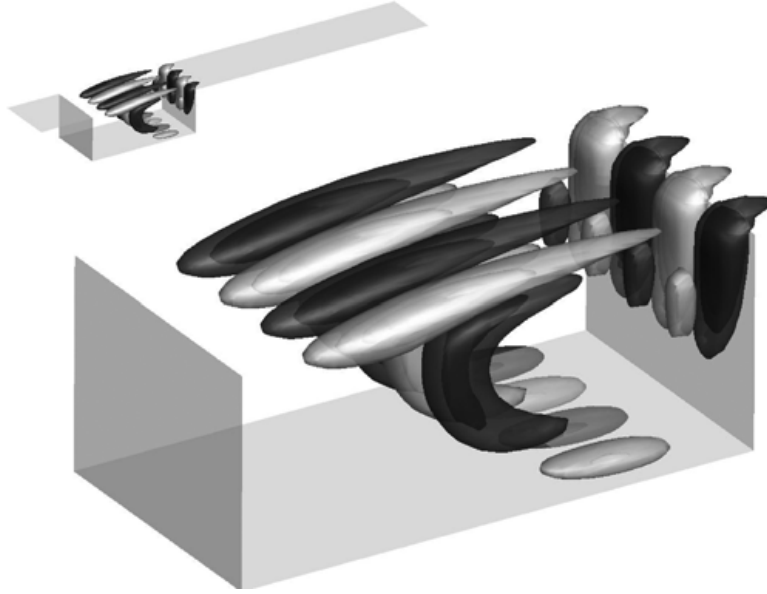
FIGURE 8. Three-dimensional visualisation of spanwise velocity at $Re_D = 2400$ and $\beta = 6$: leading disturbance obtained using BiGlobal analysis. Dark and light shadings represent positive and negative iso-values, respectively.

the water tunnel and is located $6.34D$ from the leading edge of the plate. The distance from the flat-plate water-tunnel walls is nominally $F = 225$ mm, such that $F/D = 4.5$. The results presented in the following have been obtained for two mean free-stream velocities $U_A = 29.5 \pm 0.8$ mm s^{-1} and $U_B = 47.0 \pm 0.9$ mm s^{-1}, which correspond to Reynolds numbers Re_D of 1500 and 2400, respectively. Inflow characteristics are provided in table 4.

The single-exposed image acquisitions are carried out using three synchronised CCD cameras each one with an array of 4904×3280 pixels. Such a configuration is required for a field of view spanning the cavity ($S = 500$ mm) with a high spatial resolution. The three imaged regions, each corresponding to $3.62D \times 2.42D$, partially overlap to enable merging into a single velocity field. The light source is supplied by a dual cavity Nd:YAG laser producing 120 mJ pulse^{-1}. The light sheet is set to a (z,x)-plane, parallel to the cavity bottom, located at $y = -0.1D$.

Particle image pairs are analysed using multigrid cross-correlation digital particle image velocimetry (MCCDPIV). The algorithm is described in Soria, Cater & Kostas (1999) and has its origin in Soria (1996a) and Soria (1996b). It uses an iterative and adaptive cross-correlation algorithm to increase the velocity dynamic range and reduce the random and bias error. The performance, accuracy, and uncertainty of the algorithm with applications to the analysis of a single-exposed PIV and holographic PIV (HPIV) images have been reported in Soria (1998) and von Ellenrieder, Kostas & Soria (2001).

The time interval between velocity fields is typically 3 s. This low repetition rate is however sufficient to satisfy the Shannon criterion with regard to spanwise dynamics of the inner flow. Indeed, the two investigated Reynolds numbers $Re_D = \{1500; 2400\}$ correspond to particularly low incoming velocities U_0 in water (table 4) so that sampling frequencies are $f_s D/U_0 = \{0.57; 0.39\}$, respectively. As a result, the experimental dataset is time-resolved, enabling the analysis of time series across the velocity fields.
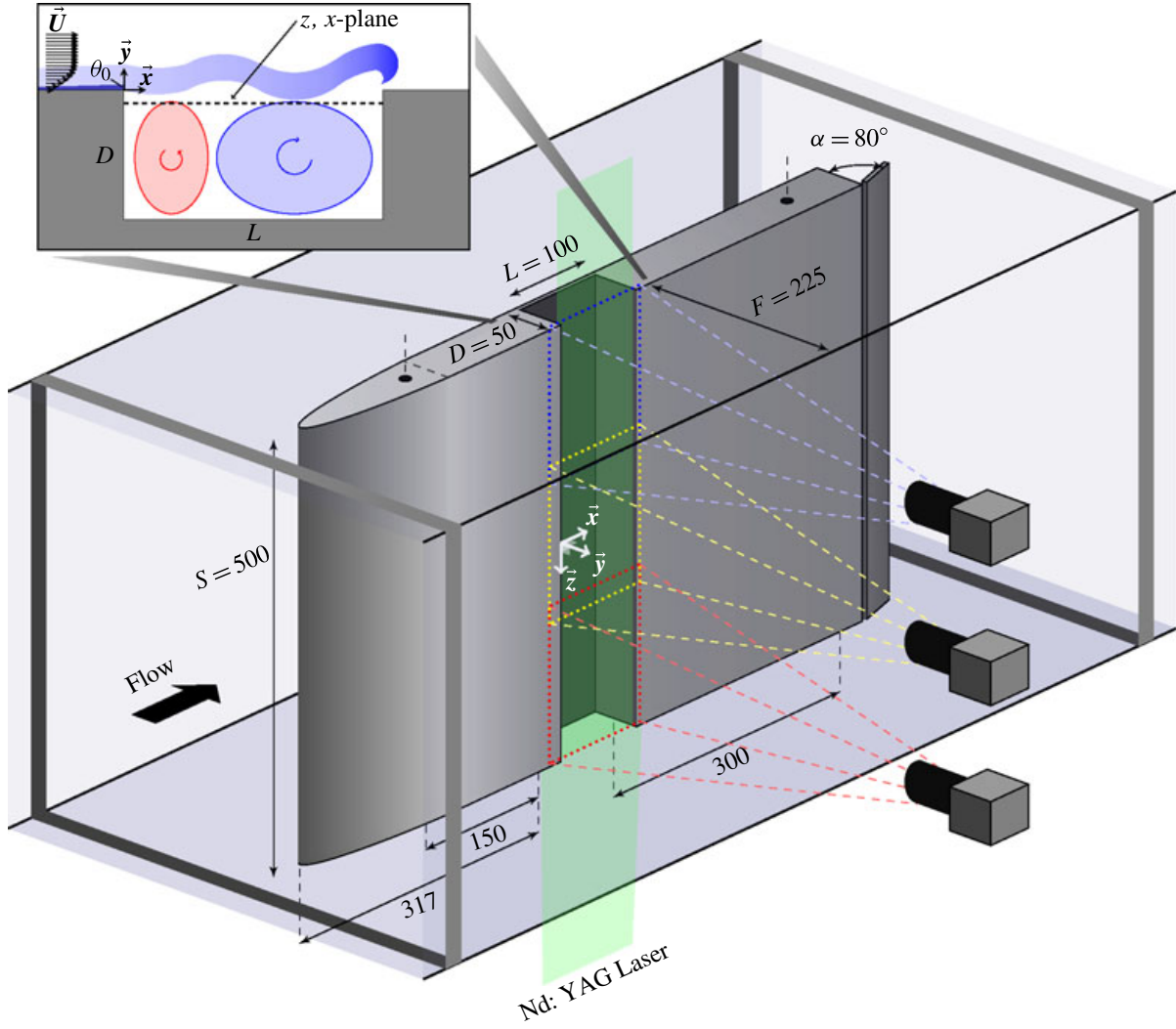
FIGURE 9. (Colour online) Sketch of the experimental set-up. Dimensions are given in millimetres. The laser sheet (at $y = -0.1 D$) is represented in a close-up on the $L = 2D$-shaped cavity. High-resolution images require three cameras to span the cavity.

	$\tilde{U}_0$ (mm s^{-1})	$\tilde{\delta}_0^*$ (mm)	$\tilde{\theta}_0$ (mm)	Re_D	$\theta_0 = \tilde{\theta}_0/D$	Re_{θ_0}
A	29.5 ± 0.8	5.59 ± 0.28	2.16 ± 0.11	1500 ± 43	0.0432 ± 0.0022	65 ± 4.9
B	47.5 ± 0.9	4.27 ± 0.18	1.70 ± 0.07	2400 ± 51	0.0340 ± 0.0015	81 ± 5.0

TABLE 4. Characteristics of the wall-bounded laminar inflow at the leading edge ($x = 0$).

3.2. *Preliminary remarks*

The time-resolved two-component, two-dimensional velocity fields can be written as

$$U(z, x, y = -0.1 D, t) = w\,e_z + u\,e_x. \tag{3.1}$$

The forthcoming analyses are applied to the cross-stream vorticity

$$\omega_y(z, x, y = -0.1 D, t) = \overline{\omega}_y(x) + \omega'_y(x, t), \tag{3.2}$$

where $\overline{\omega}_y$ is the mean vorticity and $\omega'_y(t)$ the vorticity fluctuations. The (z,x)-plane under study is just below the shear layer, which may or may not be unstable
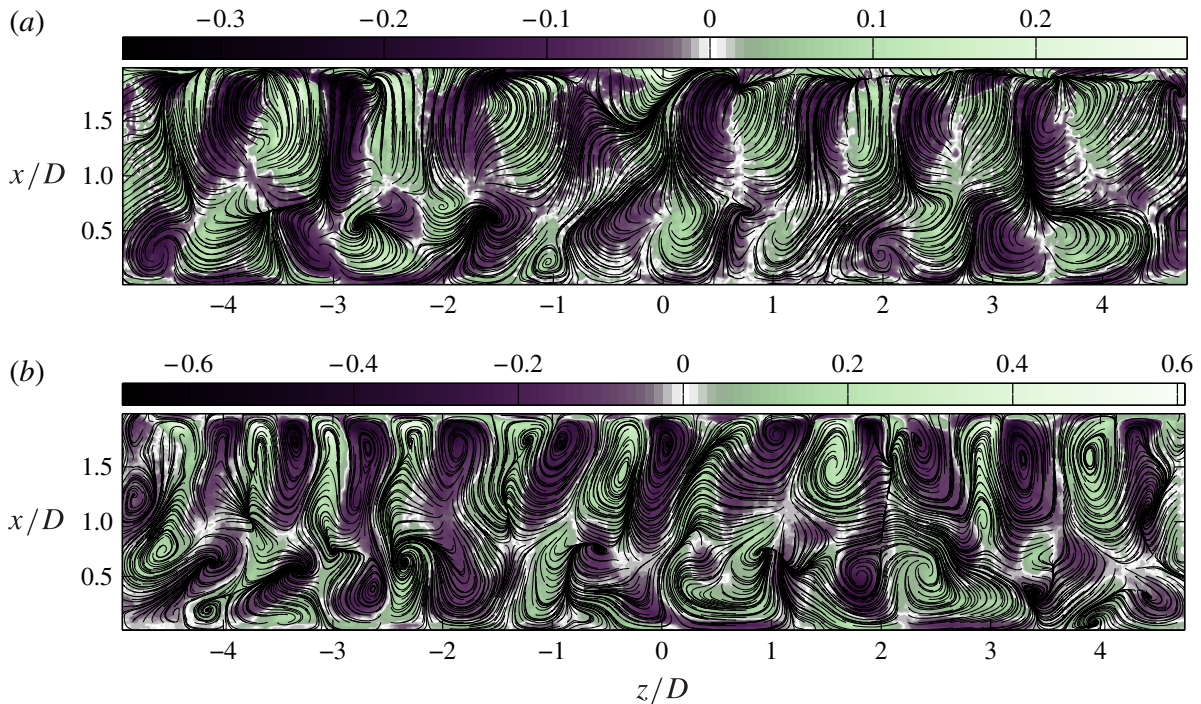
FIGURE 10. (Colour online) Examples of instantaneous fields in plane ($y = -0.1D$) for the two configurations: (a) $Re_D = 1500$, $\theta_0 = 0.0432$; (b) $Re_D = 2400$, $\theta_0 = 0.0340$. Dimensionless normal vorticity fluctuations $\omega_y' D/U_0$ are displayed in colour scales along with streamlines generated from fluctuations only (—).

depending on L/θ_0 (Rockwell & Naudascher 1979; Knisely & Rockwell 1982). Such a plane is tangent to the recirculating mean flow. The projected velocity field therefore represents most of the mean flow, with a reduced out-of-plane velocity restricted mainly to outer regions near the cavity leading and trailing edges. Examples of instantaneous vorticity fields are presented in figure 10.

As expected for such Reynolds numbers, the cavity inner flow is strongly three-dimensional: highly coherent spanwise-oscillating structures can be observed. No visible trace of shear-layer vortex shedding is found in contours of cross-stream vorticity ω_y'. Indeed, shear-layer modes are primarily two-dimensional. As such, they remain confined in the (x,y)-space, only generating spanwise vorticity ω_z'. For both cases A and B, velocity fields present large-scale structures encompassing the cavity length (figure 10). The whole inner flow experiences a spanwise oscillation. Spanwise-distributed structures of alternate vorticity appear to be closely entangled with both main and secondary recirculations. Phase evolves continuously in the spanwise direction, except for the boundaries located around $x/D \simeq 0.7$ and $x/D \simeq 1.8$. Such phase discontinuities, segregating fluctuations in the outer region of the cavity, correspond to the borders of the main recirculation crossing the extracted (z,x)-plane. That demarcation is also shown by converging streamlines which, in a slice of a three-dimensional flow, mark the position of a sink. Although they are generated with velocity fluctuations, streamlines are pulled in and stretched by an out-of-plane velocity, resulting in strong concentrations of vorticity. These features are similar to qualitative results reported in Migeon (2002) and Migeon, Pineau & Texier (2003) and suggest that centrifugal instability waves travel along the main recirculation.

For the characteristic length of the spanwise waves, preliminary observations lead to a dominant wavelength of $L_z \simeq 1$.

One must note that in contrast to numerical simulations which often use a two-dimensional geometry (periodic transversal conditions) an experimental facility implies the cavity span to be limited by Dirichlet boundary conditions,

$$\boldsymbol{q}(x, y, z = \pm S/2) = 0. \tag{3.3}$$

In the present case, cavity endwalls are the floor and ceiling of the water tunnel. The effects of such a non-periodic lateral boundary conditions will be discussed in §4.2.

3.3. *Spanwise wavelengths and statistics*

Space Fourier analysis of vorticity fluctuations ω'_y can be undertaken along the z direction to identify the spanwise wavelengths at play in the inner flow of the cavity. The main issue with a space Fourier transform applied to that system is the lack of precision in the identification of the wavenumbers. Depending directly on the length of the spanwise array, here $S/D = 10$, the dimensionless spectral step is initially $2\pi/10 = 0.63$, while wavenumbers to be resolved are of the order of 2π, that is only one order of magnitude higher. Padding zeros to spanwise arrays prior to Fourier transform computation enables decreasing the wavenumber step down to $\delta\beta = 0.32$. Statistics are then performed on spectra $|\mathscr{F}^z(\omega_y')|$. The mean spectrum $\langle\mathscr{F}^z(\omega_y')\rangle$ is averaged over various x positions (one out of four rows, that is approximately 40 spanwise arrays) and the whole set of velocity fields (more than 2000 samples for each configuration). Spectra samples used for averaging are not fully independent. Nonetheless, having approximately 80 000 spanwise arrays of different phase is large enough to get sufficient convergence in terms of Fourier transform intrinsic noise. Note also that results obtained through Fourier transform have been validated by Hilbert–Huang transform (Huang *et al.* 1998; Huang, Shen & Long 1999). The resulting spectra fairly well match Fourier power spectral densities (Basley 2012). Mean spanwise Fourier spectra are displayed for both cases in figure 11. The range and amplitude of active wavelengths grow wider and larger for case *B* than for case *A*. This denotes an increase of energy and complexity, as expected for control parameters further from the threshold of centrifugal instabilities. Both cases exhibit maximal energy around $\beta_{max} \simeq 2\pi$ (that is $L_z \simeq 1$). More particularly, the highest peak is located at $\beta_{max}(A) = 6.3$, $\beta_{max}(B) = 5.8$, respectively. These results are consistent with the literature (Chiang, Sheu & Hwang 1998; Faure *et al.* 2007; Brès & Colonius 2008; Faure *et al.* 2009). Secondary peaks appear also for case *B* around $\beta \simeq 7.5$ and $\beta \simeq 10$.

3.4. *Space–time dynamics of the flow*

The space–time dynamics of the cavity inner flow can be thoroughly characterised through a modal decomposition in time, which enables identification of the coherent structures associated with a given time scale. Indeed, when samples are time-resolved, Fourier transform can be performed along time series extracted from various points spatially distributed across the velocity fields, as described in Basley (2012). If every point of the grid is selected, one ends up with a set of complex spatial modes of dimensions equal to those of velocity fields, each associated with a Strouhal number (Rowley, Colonius & Basu 2002; Basley *et al.* 2011). Then, additional decomposition is required to identify the space scales composing each complex spatial mode under consideration.
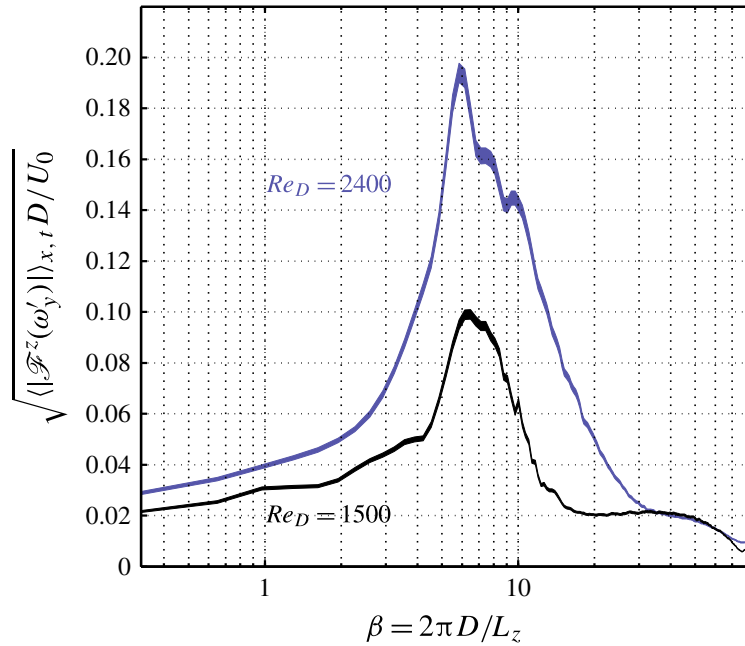
FIGURE 11. (Colour online) Space Fourier spectrum as a function of dimensionless wavenumber β, for both cases $A : Re_D = 1500$, $D/\theta_0 = 23.2$; $B : Re_D = 2400$, $D/\theta_0 = 29.4$. Fourier transform is performed on vorticity fluctuations $\omega_y' D/U_0$. To reduce boundary effects, a Hamming window is applied prior to Fourier computation. Curve thickness corresponds to the 95 %-confidence interval of Fourier calculation, integrated along x/D and snapshots for greater statistics.

3.4.1. *Characteristic frequencies*

Prior to investigation of coherent structures, a preliminary study consists of integrating in space the power spectral density performed over time series. The resulting time spectra are presented in figure 12. Fourier transform uncertainty is reduced thanks to integration over the entire field and to window averaging: the 95 %-confidence interval is approximately ± 0.12 dB using a χ^2 function. Computation windows correspond to 1130 and 1680 time units $t U_0/D$ for cases A and B, respectively. Both cases exhibit a spectrum with maximum between $0.013 \leqslant St \leqslant 0.023$, recalling what was observed in Chiang *et al.* (1998), Douay *et al.* (2011) and Basley *et al.* (2013). One observes various peaks that could either derive from independent eigenmodes or result from nonlinear interactions. They are classified in arbitrary spectral subdomains $m = [0–4]$:

$$
\begin{array}{lll}
m = 0: & St_D \sim 0^+ & \text{(steady features)} \\
m = 1: & St_D < 0.01 & \text{(slow variations)} \\
m = 2: & St_D \sim 0.02 & \text{(dominant waves)} \\
m = 3: & 0.02 \leqslant St_D \leqslant 0.03 & \text{(secondary peaks)} \\
m = 4: & St_D > 0.03 & \text{(smaller time scales)}
\end{array}
$$

Many well-defined frequencies are visible for case A ($Re_D = 1500$, $\theta_0 = 0.0431$). For instance, the peaks at $St = 0.038$ and $St = 0.057$ in case A probably correspond to harmonics of the dominant peak at $St = 0.019$. On the contrary, the spectrum of case B ($Re_D = 2400$, $\theta_0 = 0.034$) shows overall a higher background level, as expected from higher values of control parameters. As the system goes further from threshold, more modes become unstable, leading to a wider range of active frequencies.
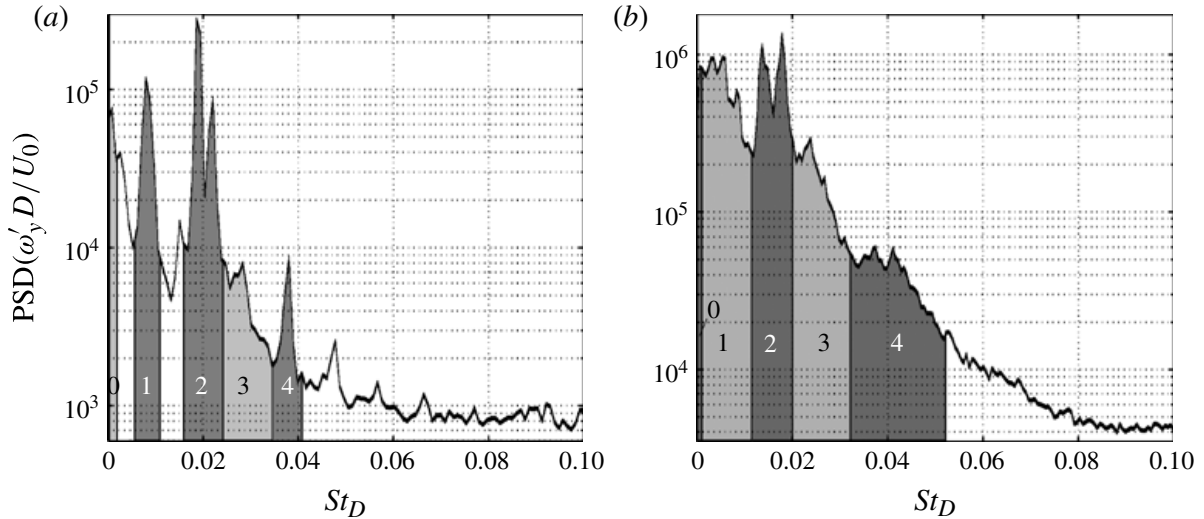
FIGURE 12. Time Fourier power spectral density performed on dimensionless cross-stream vorticity fluctuations $\omega_y' D/U_0$ for cases (*a*) A and (*b*) B. For the sake of clarity, indices $m = [0, 1, 2, 3, 4]$ correspond to arbitrary spectral subdomains in the following.

3.4.2. *Associated spatial modes*

After the space-integrated power signature, spectral analysis is extended to spatially extended time Fourier decomposition. Projecting the dataset on the exponential functions $\exp(2\pi i f_k t)$, the resulting complex spatial modes (referred to as *global Fourier modes*) are available for any Strouhal number such that

$$St_k = \frac{k}{N} \frac{D}{U_0\, \delta t} \quad \text{with } k = [-N/2, N/2], \tag{3.4}$$

with δt the time step and $N + 1$ the number of snapshots. For cases A and B, the spectral steps are $D/(N\delta t U_0) = \{13 \times 10^{-4}, 9 \times 10^{-4}\}$. Global Fourier modes associated with salient frequencies are presented in the top plots of figures 13–17. In order to identify space scales, space Fourier transforms are applied spanwise to global Fourier modes. The reader can find a schematic outline of the decomposition in Basley (2012). Spanwise Fourier analysis yields the spectra $\mathscr{F}^z(\beta, x, St_k)$, which are shown in the bottom plots of figures 13–17.

3.4.3. *Space–time modal decomposition*

Hereinafter several coherent structures revealed by time and space decompositions are investigated. For each considered time scale, space-scale distributions can help to identify the underlying phenomenon. However, it is important to remark that results are obtained from a limited number of events. In this sense, the forthcoming figures convey characteristic features of the present dataset rather than an exhaustive analysis of the inner flow which would require more extensive statistics.

Steady features ($m = 0 : St_D \sim 0^+$)

The first salient Strouhal number to be considered in figure 13(*a*) is $St = 0$, corresponding to the mean flow. By definition, its imaginary part is uniformly null. Overall, a strong two-dimensional signature ($\beta \simeq 0$) is observed close to the downstream and upstream cavity walls ($x/D \to 0$ and $x/D \to 2$). This probably represents the (steady) signature of the spanwise solid boundary conditions. On the
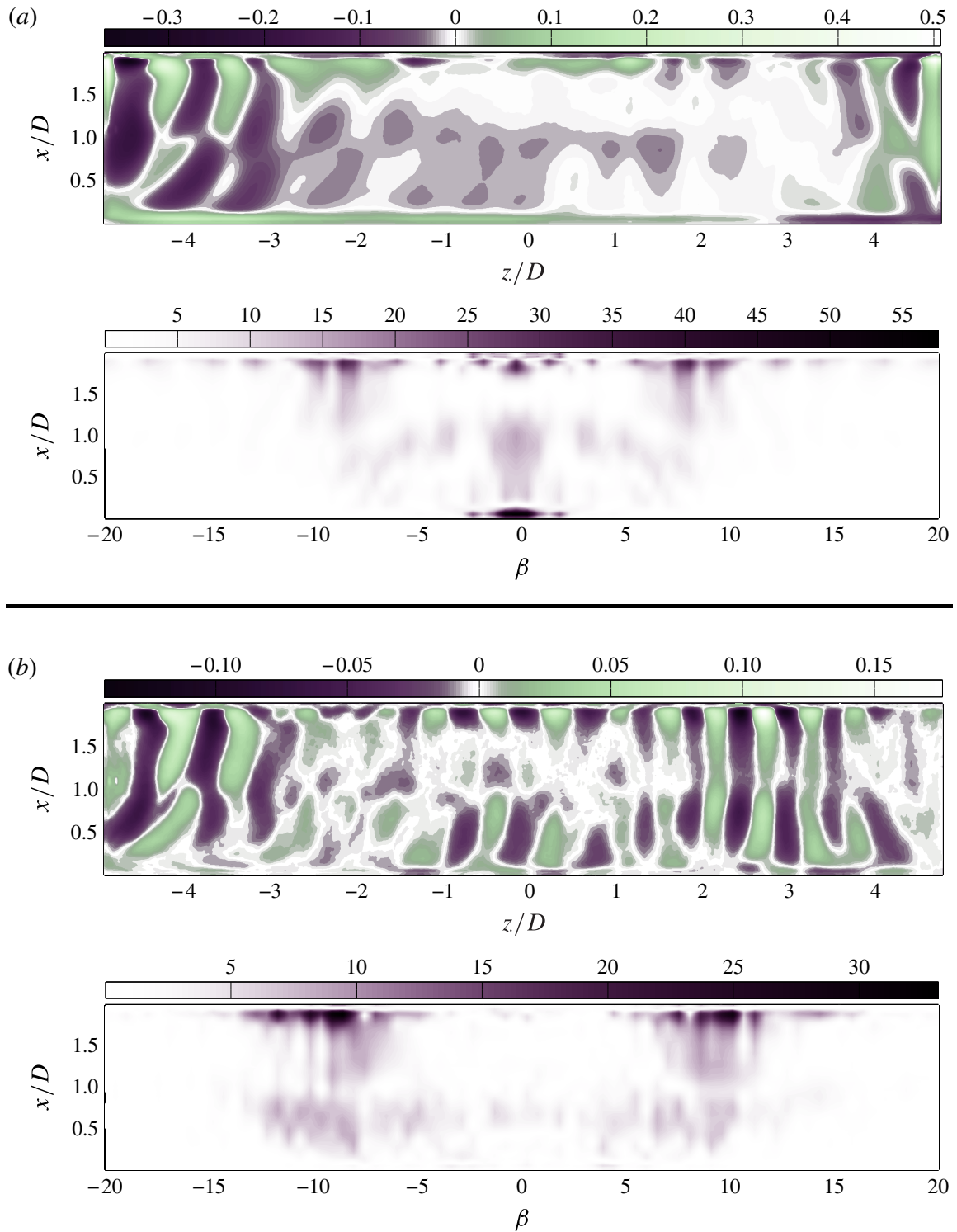
FIGURE 13. (Colour online) Global Fourier modes associated with Strouhal numbers pertaining to subdomain $m = 0$, for case B, $Re_D = 2400$, $\theta_0 = 0.0340$: (a) mean flow ($St_D = 0$), (b) $St_D = 0.002$. Top plots: real part, colours encoding vorticity $\omega'_y D/U_0$; bottom plots: spanwise spectrum $\mathscr{F}^z(\beta, x) \times 10^{-3}$.

other hand, spanwise oscillations at smaller scales $\beta \simeq 10$ ($L_z = 0.6$) are also visible near the endwalls.

As data acquisitions last for long periods (typically 20 min), experimental conditions can vary, implying slow motions in theoretically steady phenomena.
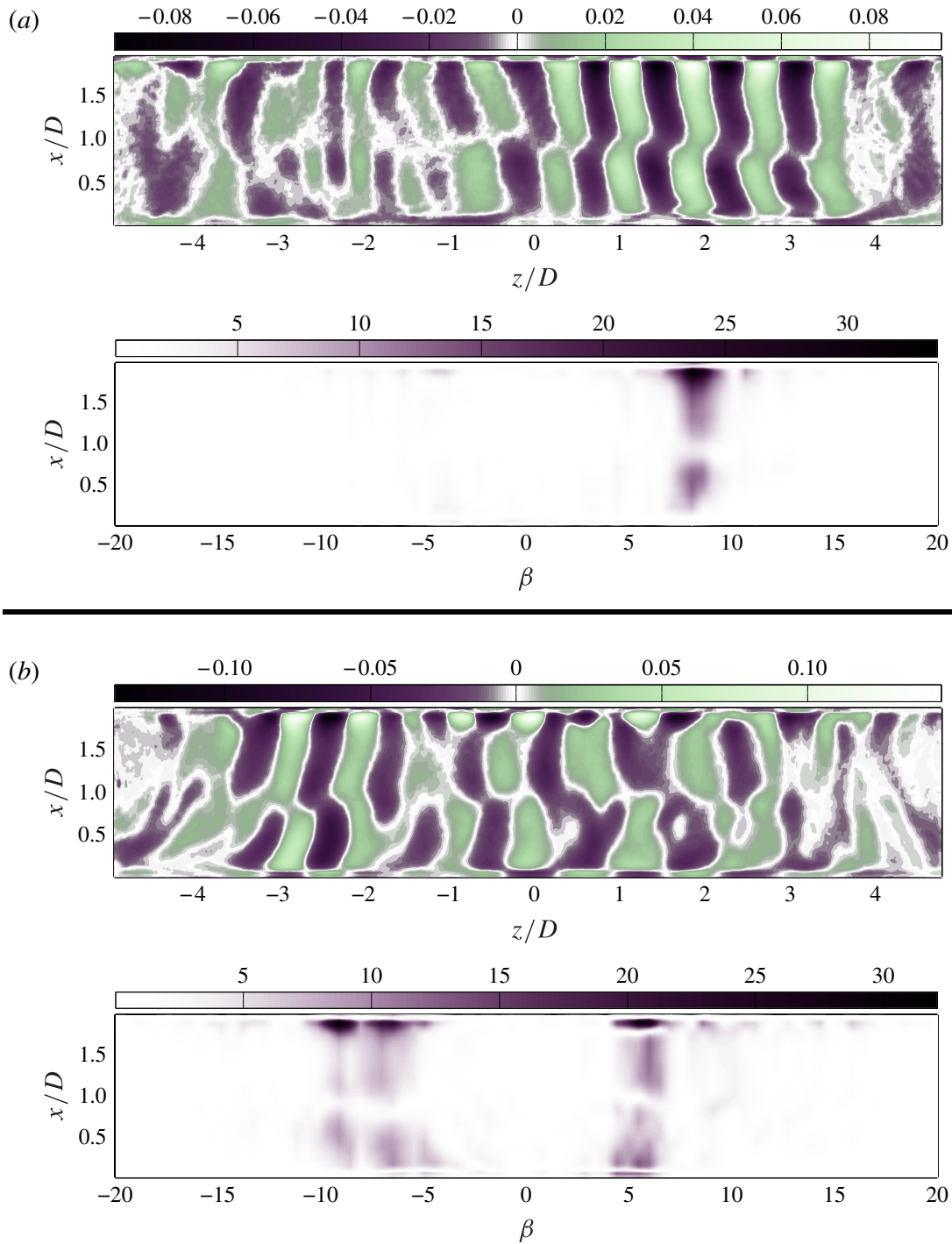
FIGURE 14. (Colour online) Global Fourier modes associated with frequencies pertaining to subdomain $m = 1$: (a) $St_D = 0.007$ for case A, $Re_D = 1500$; and (b) $St_D = 0.006$ for case B, $Re_D = 2400$. Top plots: real part, colours encoding vorticity $\omega_y' D/U_0$; bottom plots: spanwise spectrum $\mathscr{F}^z(\beta, x) \times 10^{-3}$.

Consequently, the global Fourier modes associated with the lowest Strouhal numbers can be considered as quasi-steady structures, stationary within uncertainties and experimental errors. In figure 13(b), the spatial structure associated with $St = 0.002$ for case B shows energetic spanwise oscillations distributed quite homogeneously over the entire span and broad-banded in the spectral space. Contrary to the mean flow, spanwise fluctuations correspond to small scales only. Fluctuations involve both positive and negative wavenumbers ranging continuously over $7 \leqslant |\beta| \leqslant 13$

$(0.5 \leqslant L_z \leqslant 0.9)$. From here onward, it should be noted that wavenumbers β can be either positive or negative. Positive wavenumbers correspond to right-travelling waves denoted, when necessary, with the subindex ($\rightarrow$), while left-travelling modes, associated with negative wavenumbers, will be referred to using the subindex ($\leftarrow$).

Slow variations $(m = 1 : St_D < 0.01)$

Coherent structures associated with Strouhal numbers pertaining to the spectral band $0.002 \leqslant St \leqslant 0.010$ consist of slow-travelling modes. In case A, only a narrow peak at $St = 0.007$ appears (figure 12a). Its spatial structure is displayed in figure 14(a) and indicates a travelling mode, with real and imaginary parts in quadrature of phase. The unique positive wavenumber $\beta = 8$ implies a stand-alone right-travelling wave.

While case A exhibits a single monochromatic signature, case B presents a continuum of energetic modes for frequencies up to $St = 0.010$ (figure 12b). The spatial structures are more complex as they involve multiple broader-banded travelling structures. As a result, the dynamics associated with a Strouhal number $St = 0.010$ comprises a range of wavenumbers. In figure 14(b), both left- and right-travelling waves are encountered and correspond to wavenumbers such that $-10 \leqslant \beta \leqslant -5$ and $4 \leqslant \beta \leqslant 6$, respectively. More generally, as Strouhal numbers increase, one observes a monotonic decrease of active wavenumbers from $\beta \approx 10$ to $\beta \approx 4$. Such a continuous evolution suggests these travelling waves pertain to the same underlying multicomponent family of modes.

Dominant waves $(m = 2 : St_D \sim 0.02)$

In every sample of all cases investigated during the present experimental campaign, the most energetic component of the time spectrum (figure 12) is located around $St \sim 0.02$. A global Fourier mode associated with such a peak ($St_{\leftarrow} = 0.019$) is displayed in figure 15(a). It corresponds to a highly coherent left-travelling wave encompassing half the cavity span ($z/D \leqslant 0$). For such a monochromatic wave, the spanwise Fourier spectrum shows a narrow distribution of wavenumbers around $\beta \simeq -2\pi$ ($L_z \simeq 1$). Cells organise around the recirculation, as indicated by the discontinuity of phase at $x/D = 0.8$. This dominant wave is similar to what was reported in Basley *et al.* (2013).

The dominant travelling wave is usually paired with another, that is qualitatively symmetric: a *counter-propagating wave*. The wave symmetric to $St_{\leftarrow} = 0.019$ is a right-travelling wave, with (approximately) an opposite wavenumber $\beta \simeq 2\pi$, associated with $St_{\rightarrow} = 0.023$. Its spatial structure is reported in figure 15(b).

Both counter-propagating waves are centred on the left-hand side of the cavity, where they partially overlap. As two counter-propagating waves come on top of each other, they induce interference patterns, which have been identified notably in Douay *et al.* (2011) and Basley (2012). If the counter-propagating waves had been strictly symmetric, with identical Strouhal numbers ($St_{\leftarrow} = St_{\rightarrow}$) and opposite wavenumbers ($\beta_{\leftarrow} = -\beta_{\rightarrow}$), time Fourier decomposition would have collected both waves in the same global Fourier mode, which would have consisted of a standing wave.

Secondary peaks $(m = 3 : 0.02 \leqslant St_D \leqslant 0.03)$

Considering the spectral band $0.025 \leqslant St \leqslant 0.030$, additional peaks are found for the two cases A and B, though energy levels are far lower than those of the modes of family $m = 2$. An example of a global Fourier mode associated with $St = 0.027$ in case A is provided in figure 16. Its spatial structure embracing the entire cavity span is particularly non-trivial. Spanwise space scales observed in the Fourier spectrum $\mathscr{F}^z$ are widely distributed such that $5 \leqslant |\beta| \leqslant 13$ (see the bottom plot of figure 16).
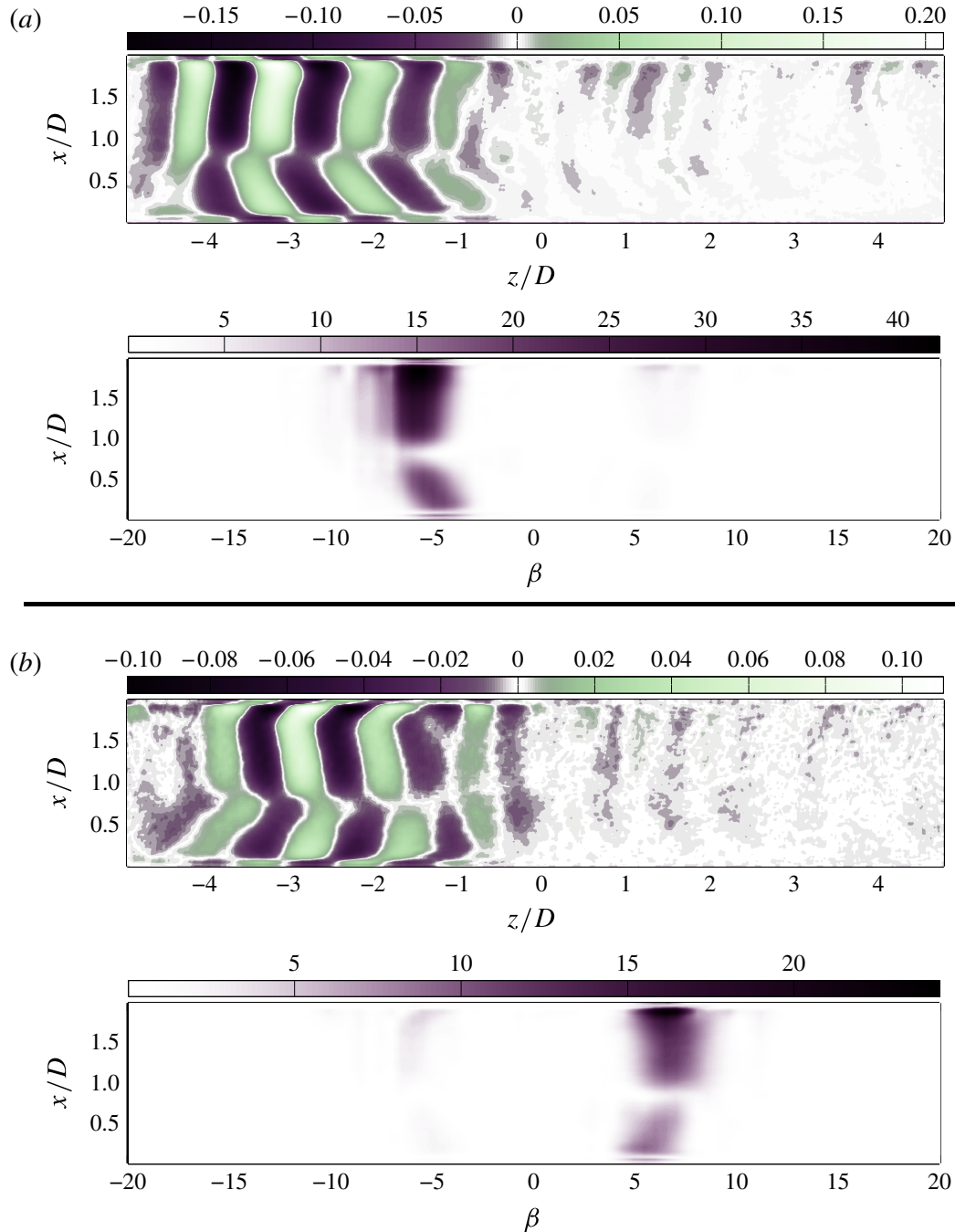
FIGURE 15. (Colour online) Global Fourier modes associated with (a) $St_D = 0.019$ and (b) $St_D = 0.023$, pertaining to spectral subdomain $m = 2$, in case $A : Re_D = 1500$, $\theta_0 = 0.0431$. Top plots: real part; bottom plots: spanwise Fourier spectrum $\mathscr{F}^z(\beta, x) \times 10^{-3}$.

Harmonics and other higher frequencies ($m = 4 : St_D > 0.03$)

Finally, there is some energy remaining in the time spectra shown in figure 12 for Strouhal numbers $St \geqslant 0.03$. Extracted at $St = 0.039$, the mode investigated in figure 17 depicts a left-travelling wave of wavenumber such that $-13 \leqslant \beta \leqslant -10$. This mode unambiguously corresponds to the first harmonic of the left-travelling dominant mode of family $m = 2$, displayed in figure 15(a). Both Strouhal number and wavenumbers are doubled and its spatial distribution exhibits a similar shape. The presence of an harmonic denotes the nonlinear saturation of the dominant mode (family $m = 2$) at $St_{\leftarrow} = 0.019$.
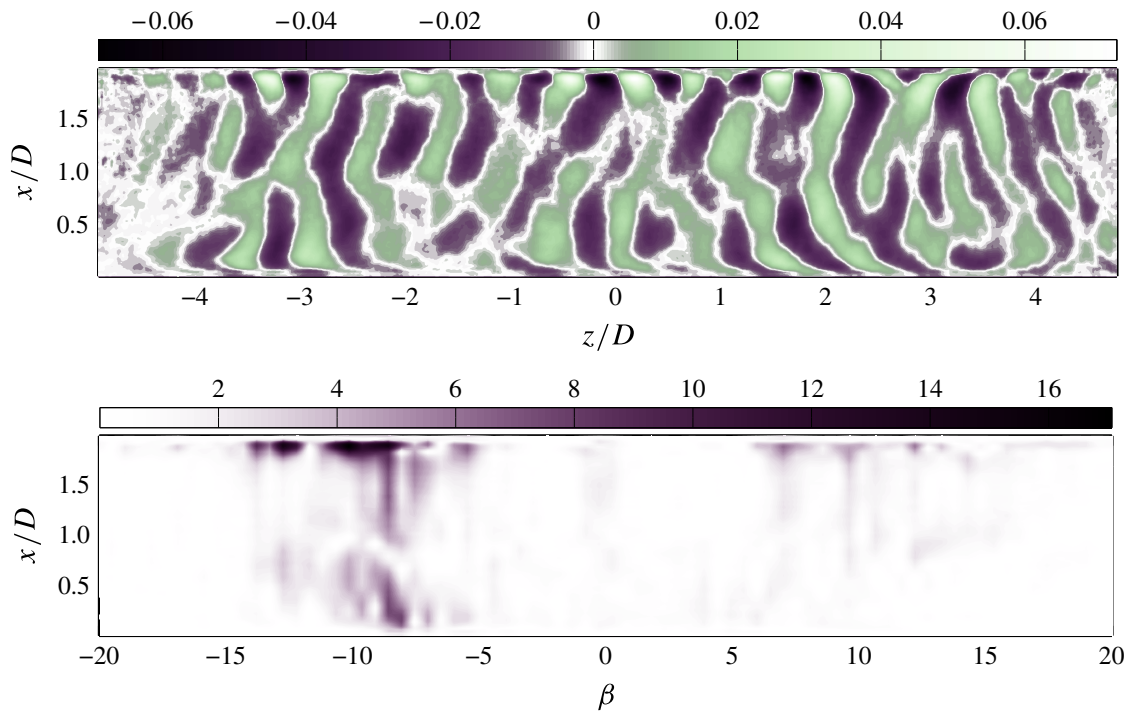
FIGURE 16. (Colour online) Global Fourier mode associated with $St_D = 0.027$ ($m = 3$) for case $B : Re_D = 2400$, $\theta_0 = 0.0340$. Top plot: real part; bottom plot: spanwise Fourier spectrum $\mathscr{F}^z(\beta, x) \times 10^{-3}$.
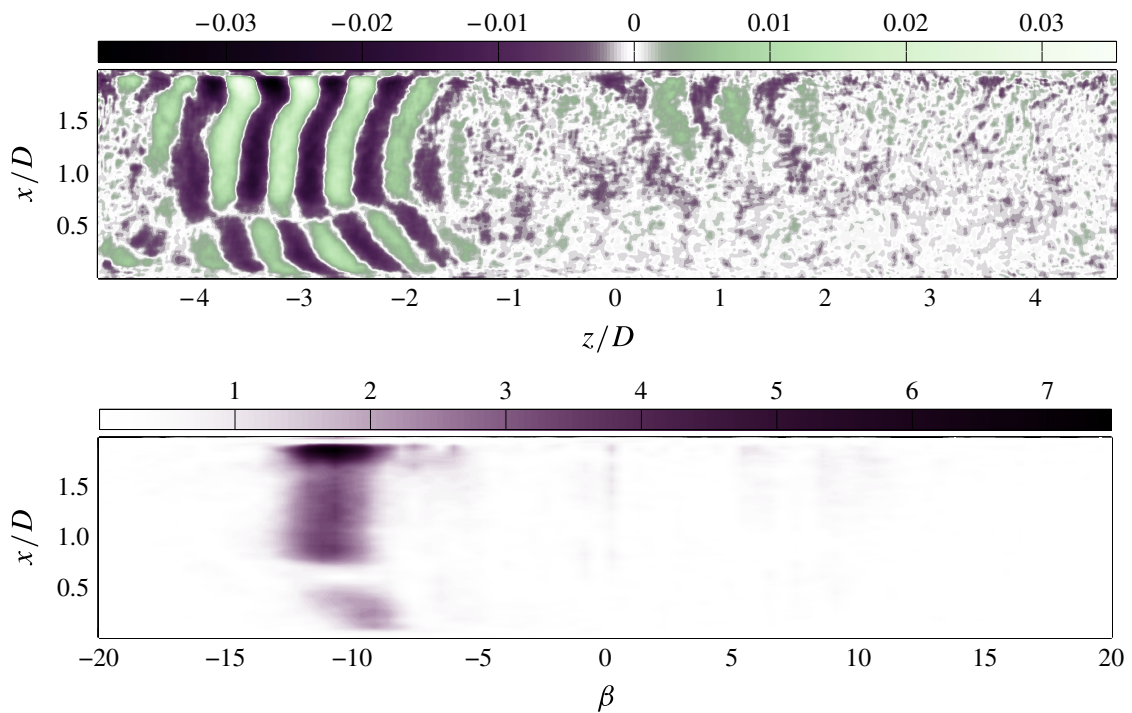

FIGURE 17. (Colour online) Global Fourier mode associated with $St_D = 0.039$ ($m = 4$) for case $A : Re_D = 1500$, $\theta_0 = 0.0431$. Top plot: real part; bottom plot: spanwise Fourier spectrum $\mathscr{F}^z(\beta, x) \times 10^{-3}$.

3.5. *Synthesis of experimental results*

3.5.1. *Counter-propagating waves*

In spite of different control parameters, cases *A* and *B* both show highly coherent travelling waves as the most salient dynamics of the inner flow in the saturated state. In every sample under study, the dominant space scale $|\beta| \simeq 2\pi$ is associated with a pair of counter-propagating waves corresponding to Strouhal numbers $0.013 \leqslant St \leqslant 0.023$. These waves cover the whole cavity length, with a phase discontinuity around $x/D = 0.8$ between the two recirculating cells. When two travelling waves coexist, they can locally overlap and therefore produce interference (beating). Given that wavenumbers are basically identical for all those waves, Strouhal numbers directly depend on the phase velocities of the travelling waves. As Strouhal numbers get lower near the endwalls, the propagation could be slowed down by solid boundary conditions. Such a phenomenon was suggested by Shankar & Deshpande (2000) who reported a braking of the base flow due to endwalls and lid-driven cavity flows. This matter will be developed in §4.2.

3.5.2. *Broad-banded structures*

For certain frequencies, the saturated dynamics of the inner flow show broad-banded structures: a wide range of spanwise space scales, all associated with a narrow range of Strouhal numbers (especially in case *B*). Such a signature is observed for Strouhal numbers tending to zero, for which Fourier modes correspond to wavenumbers in the range $7 \leqslant |\beta| \leqslant 14$. Similarly, spatial structures associated with $St \approx 0.025$ show even more widely distributed wavenumbers $5 \leqslant |\beta| \leqslant 15$.

3.5.3. *Continuum in case B*

The time spectrum is particularly rich in case *B*. The most characteristic feature of that richness is the continuum of modes observed for Strouhal numbers up to 0.01. This continuum represents a wavepacket consisting of travelling waves ranging from slow-moving small-scale structures ($\beta \simeq -10$, $St \simeq 0.003$) to fast-moving large-scale structures ($\beta \simeq -4$, $St \simeq 0.01$).

4. Discussion

The BiGlobal stability analysis and velocity experimental measurements do not strictly highlight the same state of the system. First, linear stability analysis (§2) is concerned with the onset and the nature of the flow instabilities whereas the experiments (§3) deal with the final state of nonlinearly saturated dynamics. Furthermore, BiGlobal analysis involves an ideal noiseless two-dimensional basic flow with periodic spanwise boundary conditions, as opposed to the real conditions and confinement of the experiments, which might change the stability properties of the flow. In addition, measurements only give access to partial imperfect information, with uncertainties, being also only a modelling of a real engineering problem to be compared with the complete three-dimensional structure of the eigenmodes of the flow.

However, from merging those different viewpoints comes a further understanding of the mechanisms governing the evolution of the system, from the theoretical onset of centrifugal instabilities to the real flow.

4.1. *Validity of eigenmodes in the saturated regime*

The forthcoming discussion mainly relies on figure 18, which presents a side-by-side description of case *B* ($Re_D = 2400$, $\theta_0 = 0.0340$) from both points of view: linear stability analysis and experimental measurements. Nominal case *B* presents a greater variety of linearly unstable modes (figure 2) than case *A*, for which the control parameters are less critical ($Re_D = 1500$, $\theta_0 = 0.0432$). Indeed, case *B* reveals richer dynamics since it leads to a flow that is a combination of a greater number of different structures. As a result, the features discussed hereinafter, regarding the intrinsic instabilities in the permanent regime, apply similarly to case *A* in a simpler manner.

In figure 18 letters in dark squares and dark dots (red online) refer to results predicted using BiGlobal analysis while letters in circles and shaded regions (blue online) symbolise results from the experimental campaign. The series of dots in figure 18(*a*) denote the branches of eigenvalues corresponding to growing disturbances, represented in the (β, St_D)-plane. Four of these eigenvalues are identified with letters (A, B, C and D) inside a square. Letter D corresponds to $\beta = 11.8$, the wavenumber of maximum amplification for branch I, and letter A to $\beta = 6.3$, the wavenumber associated with the second local maximum of amplification of the same branch (see figures 2 and 3 for more details).

Letter C points to two different values of β in the most unstable disturbance, Mode II: $\beta = 12$ corresponding to maximum amplification in the stationary branch II(a) and $\beta = 8.5$ just before the bifurcation in the oscillatory branch of the same Mode II(b). Finally, letter B indicates another mode of the same branch II(b), but with different properties ($\beta = 7.8$, $St = 0.0054$).

Also in figure 18(*a*), the shaded regions are a qualitative representation of the energy in this (β, St_D)-plane according to the space–time Fourier analysis of the experimental data. Dashed lines, labelled by circled letters A–D, denote four characteristic frequencies of the Fourier spectrum.

In figure 18(*b,c*), the spatial modes associated with the four letters A–D are depicted through their streamwise and spanwise velocity fields. The Fourier modes (figure 18*b*) and BiGlobal eigenmodes (figure 18*c*) are discussed side-by-side. To that end, velocity profiles have been extracted from a three-dimensional reconstruction of the eigenmodes in the plane $y = -0.1D$ (as in the experiments). For the sake of clarity each BiGlobal mode is only depicted in the area of most resemblance with the experimental Fourier mode.

In order of increasing Strouhal number, the first modes to be considered are those corresponding to steady disturbances (denoted by letter C in figure 18). According to linear analysis there is a range of wavenumbers ($9 \lesssim \beta \lesssim 19$) for which the stationary branch of Mode II is unstable. In the experiments, wavenumbers for steady structures match the BiGlobal predictions, but with a tendency to concentrate near the endwalls of the rig. Within the uncertainty of experiments and in real conditions, 'quasi-steady' dynamics can also be considered with regard to stationary eigenmodes. For instance, the structures present on the right side of the Fourier mode (C) in figure 18(*b*) resemble those predicted by the linear stability analysis in the stationary branch II(a). The most coherent and energetic structures correspond to $\beta \simeq 12$, which is the wavenumber for maximum amplification according to BiGlobal analysis. Other coherent structures visible near the left wall in the experiments for the same Fourier mode (C) exhibit a tilted shape, characteristic of travelling waves. These slow-moving structures probably belong to the oscillatory branch of the same mode II(b) close to the bifurcation. Indeed, streamwise and spanwise velocity components of the
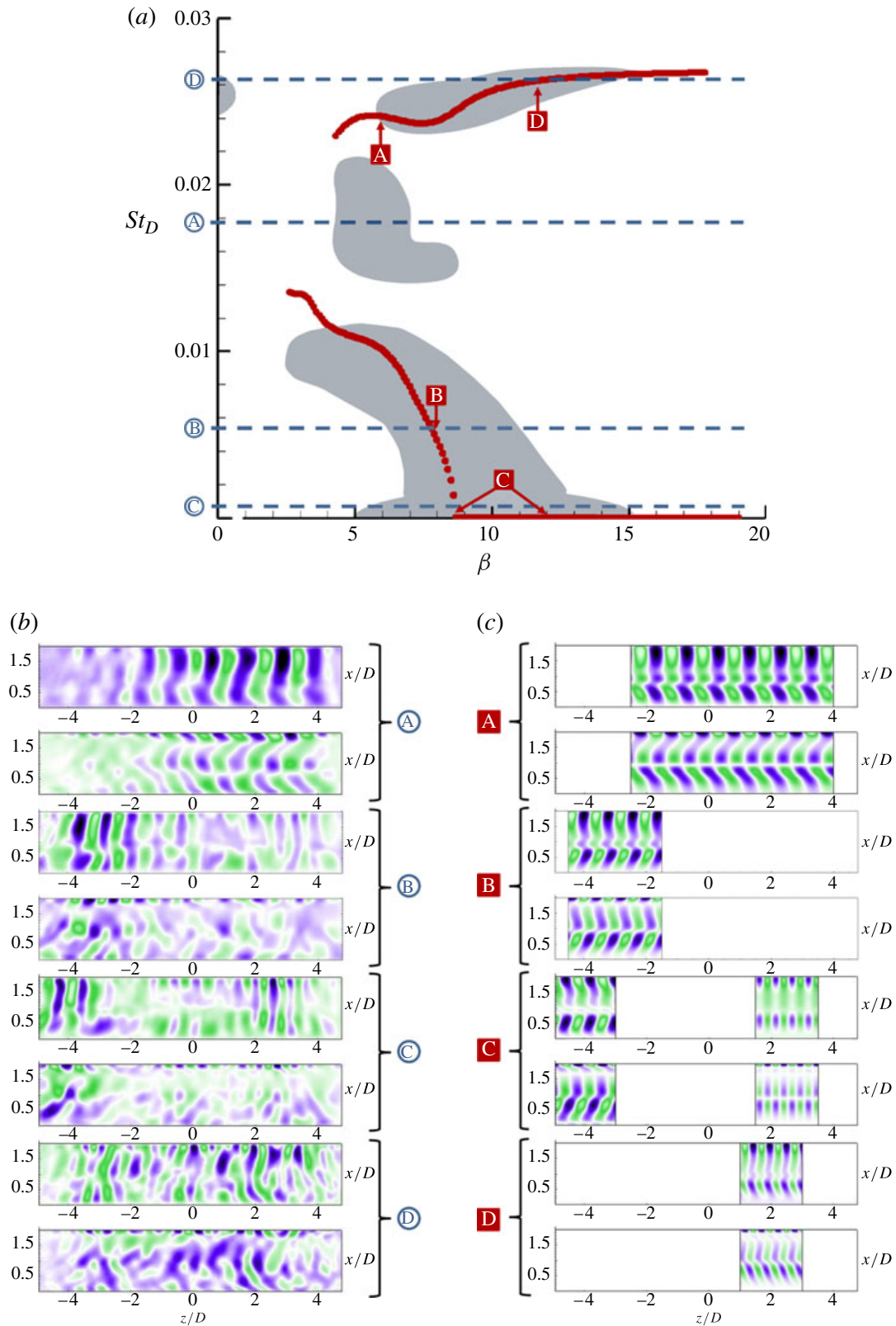
FIGURE 18. (Colour online) Main flow features at $Re_D = 2400$ for both experimental and linear stability analysis. (a) BiGlobal unstable eigenvalues (dots) and qualitative schematic depiction of the most energetic modes in the experiments (shades) in the (β, St_D)-plane. (b,c) Velocity fields related to the four representative modes highlighted in (a): (b) corresponds to global Fourier modes from the experimental dataset; (c) presents the reconstructed flow using BiGlobal analysis. For each mode, streamwise velocity (top plot) and spanwise velocity (bottom plot) are shown.

linearly reconstructed flow present a qualitative morphological similarity with the experimental data in the region of the cavity where the mode appears. However, the coherent structures in the experiments are not dominant in terms of energy, whereas the corresponding BiGlobal eigenmodes are associated with the largest growth rates. It is important to point out that the mode with the highest growth rate in linear analysis does not necessarily have to be the most energetic mode in the saturated regime.

The oscillatory branch II(b) remains unstable as the Strouhal number increases, while the associated spatial wavenumber decreases. This disturbance seems to correspond to a continuum of modes observed in the experiments. For instance, the dynamics depicted in the Fourier mode (B) exhibit energetic coherent structures consistent with the eigenmodes (B) existing in the same range of space–time scales, except for a slight reduction of the Strouhal numbers. As expected, the velocity fields are morphologically similar to those previously observed in modes (C), given that it is the same branch with a different wavenumber.

From the BiGlobal analysis, the most linearly unstable oscillatory branch is Mode I, for both case A ($Re_D = 1500$) and case B ($Re_D = 2400$), corresponding to Strouhal numbers such that $St_D \simeq 0.025$. In case B, although the fastest-growing eigenmode is associated with $\beta = 11.8$ and corresponds to $St_D = 0.027$, a broad range of spanwise waves are actually unstable (for $4 \leqslant \beta \leqslant 18$). The reconstruction of the most unstable configuration of this branch is shown on figure 18(*c*), denoted with letter D. From the experiments, the frequency band $St_D \simeq 0.027$ is associated with broad-banded dynamics involving wavenumbers in the range $5 \leqslant |\beta| \leqslant 15$. The global Fourier mode (D) seen in figure 18(*b*) exhibits many patterns recalling the spatial structure of various eigenmodes of branch I. This suggests that the saturated dynamics observed in the experiments are composed of a continuum of waves derived from intrinsic instabilities pertaining to the unstable branch of Mode I.

Finally, the most prominent dynamics revealed by experimental datasets are associated with Strouhal numbers such that $0.013 \leqslant St_D \leqslant 0.023$. In both cases A and B, these dominant features consist of highly coherent right- or left-travelling waves, corresponding to a well-defined wavelength $\lambda \simeq D$ ($|\beta| \simeq 2\pi$). These structures have been encountered as pairs of counter-propagating waves or as a stand-alone pulsating pattern when and where two waves overlap. A global Fourier mode of such a travelling wave can be favourably compared to an eigenmode from the branch I corresponding to the same $\beta = 2\pi$, as seen with (A) in figure 18. In fact, the velocity fields are qualitatively analogous in a wide section of the $y = -0.1D$ plane. However, the Strouhal numbers exhibited by the saturated dynamics do not correspond to any linearly unstable eigenvalues, neither from branch I ($St_D \simeq 0.025$) nor branch II(b) ($St_D < 0.010$). Such a discrepancy between BiGlobal eigenmodes and Fourier modes extracted from the real flow in the permanent regime is caused either by nonlinearities or by the effects of solid boundary conditions on the stability properties of the base flow.

4.2. *Effects of three-dimensional boundary conditions*

As opposed to the two-dimensional base flow around which the linear stability analysis is performed, the real flow investigated experimentally involves solid boundary conditions caused by endwalls located at $z = \pm 5D$. Such boundary conditions probably lead to the creation of Bödewadt (Ekman-like) layers of opposite sign near both endwalls. The effect of endwall layers on the centrifugal instabilities in cavity flows

was observed first in lid-driven cavity flows (Koseff & Street 1984*c*,*b*,*a*; Chiang *et al.* 1998; Shankar & Deshpande 2000; Albensoeder *et al.* 2001; Albensoeder & Kuhlmann 2006). Endwall layers are usually modelled as slow-rotating centripetal disks making the junction between the main recirculation and rigid boundaries. Guermond *et al.* (2002) and Migeon *et al.* (2003) notably demonstrated that Bödewadt layers inject momentum through the centreline of the main recirculation. In the case of confined flows such as lid-driven cavities, Bödewadt layers would hence draw the outer edge of the inner flow from the mid-span region towards the endwalls. This would imply a spanwise drift of the centrifugal instability vortices, which coil along the outer region of the main flow, and a consequent increase of the effective Strouhal number, which is not seen here.

Similar dynamics have been observed by Faure *et al.* (2007, 2009) for open cavities of aspect ratio around $L/D \leqslant 1.25$. For such geometries, the most linearly unstable perturbation over the two-dimensional base flow is known to be a stationary disturbance (Brès & Colonius 2008; de Vicente 2010; Meseguer-Garrido *et al.* 2014). On the other hand, for larger L/D ratios the more complex geometry of the main recirculation vortex results in increasing growth rates of oscillatory eigenmodes. Unlike steady modes, these oscillatory modes become intrinsically travelling waves. Effects of endwalls are hence more difficult to foresee.

A second effect regarding the effect of the walls was described by Shankar & Deshpande (2000). The authors observed the discrepancy between the three-dimensional and two-dimensional velocity profiles for increasing Reynolds numbers due to the influence of endwall vortices. These vortices not only provoke an increase in the spanwise flow but also slow down the main centrifugal recirculation on the cavity, and that braking increases with Reynolds number.

So, the confinement causes the decrease in the velocity of the centrifugal perturbation, forcing the stability properties of the base flow to change. Indeed, Brès & Colonius (2008) have asserted that, at the first-order, the Strouhal numbers associated with oscillatory eigenmodes are conditioned by the time required for a perturbation to travel along the recirculation. From that, a deceleration due to Bödewadt layers could decrease the intrinsic frequency of the spanwise waves coiling onto the recirculation, despite the influence of the drift. This effect would become stronger for waves closer to the endwalls. Such an hypothesis could explain the difference in the Strouhal numbers between BiGlobal eigenmodes and Fourier modes for the most energetic experimental mode (A) in figure 18. Figure 19 shows a comparison between the streamwise velocity profiles in the experimental $y/D = -0.1$ plane for the base flow for the linear analysis and the mean flow in the experiments. Both cases A and B are shown, taking into account the uncertainties of the measurements. It can be seen that, as expected, the experimental values of the velocity are smaller, suggesting a braking in the main vortex. Also, this reduction of the velocity is greater in the higher Reynolds number case, which is consistent with the findings in Shankar & Deshpande (2000). This means that the braking phenomenon is a plausible explanation of the reduced Strouhal numbers reported in the experiments.

4.3. *On the symmetry breaking*

The nonlinearly saturated flow exhibits asymmetries, which are, by definition, absent from the (periodic) eigenmodes obtained through BiGlobal analysis. In particular, one may wonder why the counter-propagating dominant waves are not symmetrical.
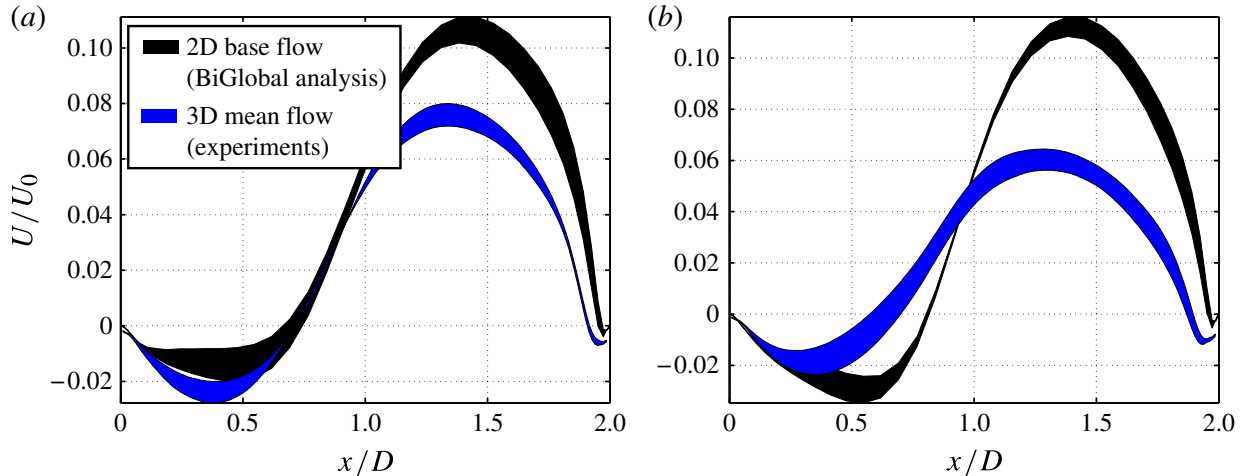
FIGURE 19. (Colour online) Streamwise profiles of streamwise velocity U/U_0 for (*a*) case A ($Re_D = 1500$) and (*b*) case B ($Re_D = 2400$). The profile of the two-dimensional base flow used by BiGlobal analysis is extracted from the range $-0.12 \leqslant y/D \leqslant -0.09$ (black), to represent the uncertainty in the position and thickness of the laser sheet. The profile of the three-dimensional mean flow, experimentally measured in the z,x-plane at $y = -0.1D$ is extracted from the range $-3 \leqslant z/D \leqslant 3$ (grey, blue online), to take into account spanwise variations.

Two plausible explications arise to justify this phenomenon. The symmetry breaking may be caused by facility-dependent effects or be inherent to the sensitivity of the flow to initial conditions.

As always, experimental conditions are characterised within uncertainties. The sources of possible experimental bias that could lead to spanwise asymmetries are: (*a*) an imperfect cavity geometry, or a crooked velocity profile due to (*b*) water-tunnel design or (*c*) angular discrepancy in cavity orientation.

Uncertainties (*a*) and (*b*) constitute systematic biases. They are ruled out since asymmetry changes from one recording to another. On the other hand, (*c*) is concerned with the alignment of the rig with the z-axis (see figure 9 for a sketch of the set-up). That alignment could vary by approximately ± 1 mm over the span $S = 500$ mm, corresponding to an angular discrepancy of $\pm 0.11°$. Such an uncertainty of only $\pm 0.1\%$ cannot alone explain the symmetry breaking. Consequently, an intrinsic sensitivity of the dynamics should rather be considered.

In fact, the reconstructed flow from stability analysis gives no preference to left-travelling, right-travelling or pulsating structures. The smallest variation in the initial conditions hence causes the real flow to break symmetries by selecting a particular pattern.

5. Concluding remarks

The main goal of this work is to use both linear stability analysis and experiments to cover the evolution of centrifugal instabilities in an open cavity flow from their onset to their observation within the nonlinearly saturated state. The intrinsic stability properties of the two-dimensional base flow are fully investigated through an extensive study of the parameter space and the features changed by nonlinear effects or/and real boundary conditions are identified and studied.

The BiGlobal analysis has been validated with respect to reference results from the literature. It also refined and developed the scope of those pioneering

works by tracking the neutral stability curve of each eigenmode within the fully extended parameter space. The flow is unstable with respect to four branches of eigenvalues corresponding either to a broad-banded family of steady structures (the stationary branch of Mode II) or a continuum of spanwise-travelling waves. The three-dimensional organisation associated with each family of eigenmodes has been identified and characterised, thus allowing some of the main agents involved in the real flow to be determined in advance with low computational cost.

On the other hand, the experimental investigation of the real flow in the permanent regime brings more insight into the dynamics that are actually selected by the real flow beyond the linear transient growth, and once real boundary conditions are set. Experimental measurements of centrifugal instabilities remain challenging in open cavities, since those three-dimensional dynamics involve particularly low frequencies and are greatly perturbed by the normally unstable shear layer above the cavity. In the present work, time-resolved high-resolution PIV measurements were performed in a spanwise plane parallel to the bottom of the cavity. Applying space-extended time-Fourier transform to such experimental data allowed the identification of the coherent structures associated with any given Strouhal number. The hypothesis of spanwise waves has been confirmed by experimental results, with dynamics in the range of unstable wavenumbers predicted by linear stability analysis. Most of the eigenmodes were recovered within the real flow, in spite of different lateral boundary conditions.

It must be noted that eigenmodes are recovered only locally, and that they can be distorted. Indeed, the saturated dynamics is strongly modulated in amplitude, resulting in local states, and those states change with time, that is, spanwise waves can also become more or less dominant in terms of energy at different times. In BiGlobal analysis, travelling eigenmodes have some degrees of freedom: the composition of the real and imaginary part of the eigenmodes can form structures that travel right, left, or that pulsate without shifting. Additional conditions in the real flow, such as confinement, noise in the upstream flow, etc., take away that degree of freedom, and a concrete structure is formed. In the case of several of those modes locally coexisting, they can overlap to produce interference and standing waves can appear.

In the saturated flow the fastest growing family of steady eigenmodes II(a) is fairly well recovered as broad-banded spatial structures associated with the slowest dynamics (for $St \to 0$). Similarly, the branch of Mode I corresponds to broad-banded dynamics at $0.025 \leqslant St \leqslant 0.03$. On the other hand, spanwise waves associated with Strouhal numbers $St \leqslant 0.01$ exhibit narrower ranges of space scales, which is consistent with eigenmodes from branch II(b). The most energetic travelling waves observed in the permanent regime, though, partially depart from the linear stability results. Those highly coherent waves strikingly resemble the eigenmodes from the unsteady low-β branch of Mode I. However, they are associated with time scales such that $0.013 \leqslant St \leqslant 0.023$, lower than the Strouhal numbers predicted for those structures by the linear stability analysis. The hypothesis presented here to explain those different time scales relies upon the modification of the base-flow due to confinement effects. The presence of endwalls could be responsible for a braking of the main recirculation, leading to slower travelling waves in the three-dimensional base flow, relatively to the two-dimensional base flow used by BiGlobal stability analysis.

REFERENCES

ALBENSOEDER, S. & KUHLMANN, H. C. 2006 Nonlinear three-dimensional flow in the lid-driven square cavity. *J. Fluid Mech.* **569**, 465–480.

ALBENSOEDER, S., KUHLMANN, H. C. & RATH, H. J. 2001 Three-dimensional centrifugal-flow instabilities in the lid-driven-cavity problem. *Phys. Fluids* **13**, 121–135.

BARKLEY, D. 2006 Linear analysis of the cylinder wake mean flow. *Europhys. Lett.* **75** (5), 750–756.

BASLEY, J. 2012 An experimental investigation on waves and coherent structures in a three-dimensional open cavity flow. PhD thesis, Université Paris-Sud, Nash University.

BASLEY, J., PASTUR, L. R., LUSSEYRAN, F., FAURE, T. M. & DELPRAT, N. 2011 Experimental investigation of global structures in an incompressible cavity flow using time-resolved PIV. *Exp. Fluids* **50** (4), 905–918.

BASLEY, J., PASTUR, L. R., DELPRAT, N. & LUSSEYRAN, F. 2013 Space–time aspects of a three-dimensional multi-modulated open cavity flow. *Phys. Fluids* **25** (6), 064105.

BRÈS, G. A. & COLONIUS, T. 2008 Three-dimensional instabilities in compressible flow over open cavities. *J. Fluid Mech.* **599**, 309–339.

CATTAFESTA III, L. N., GARG, S., KEGERISE, M. S. & JONES, G. S. 1998 Experiments on compressible flow-induced cavity oscillations. *Proceedings of the 29th Fluid Dynamics Conference, AIAA Paper 98-2912.*

CHIANG, T., SHEU, W. & HWANG, R. 1998 Effects of the Reynolds number on the eddy structure in a lid-driven cavity. *Intl J. Numer. Meth. Fluids* **26**, 557–579.

DOUAY, C. L., GUÉNIAT, F., PASTUR, L., LUSSEYRAN, F. & FAURE, T. M. 2011 *Instabilités centrifuges dans un écoulement de cavité: décomposition en modes dynamiques*, Comptes-Rendus des Rencontres du Non-linéaire, vol. 14, pp. 47–52. Non-Linéaire Publications.

VON ELLENRIEDER, K., KOSTAS, J. & SORIA, J. 2001 Measurements of a wall-bounded turbulent, separated flow using HPIV. *J. Turbul.* **2**, 1–15.

FAURE, T. M., ADRIANOS, P., LUSSEYRAN, F. & PASTUR, L. R. 2007 Visualizations of the flow inside an open cavity at medium range Reynolds numbers. *Exp. Fluids* **42** (2), 169–184.

FAURE, T. M., PASTUR, L. R., LUSSEYRAN, F., FRAIGNEAU, Y. & BISCH, D. 2009 Three-dimensional centrifugal instabilities development inside a parallelepipedic open cavity of various shape. *Exp. Fluids* **47** (3), 395–410.

GONZALEZ, L. M., AHMED, M., KÜHNEN, J., KUHLMANN, H. C. & THEOFILIS, V. 2011 Three-dimensional flow instability in a lid-driven isosceles triangular cavity. *J. Fluid Mech.* **675**, 369–396.

GUERMOND, J.-L., MIGEON, C., PINEAU, G. & QUARTAPELLE, L. 2002 Start-up flows in a three-dimensional rectangular driven cavity of aspect ratio 1:1:2 at $Re = 1000$. *J. Fluid Mech.* **450**, 169–199.

HUANG, N. E., SHEN, Z. & LONG, S. R. 1999 A new view of nonlinear water waves: the Hilbert spectrum. *Annu. Rev. Fluid Mech.* **31**, 417–457.

HUANG, N. E., SHEN, Z., LONG, S. R., WU, M. C., SHIH, H. H., ZHENG, Q., YEN, N.-C., TUNG, C. C. & LIU, H. H. 1998 The empirical mode decomposition and Hilbert spectrum for nonlinear and non-stationary time-series analysis. *Proc. R. Soc. Lond.* A **454**, 903–995.

KEGERISE, M. A., SPINA, E. F., GARG, S. & CATTAFESTA III, L. N. 2004 Mode-switching and nonlinear effects in compressible flow over a cavity. *Phys. Fluids* **16**, 678–687.

KNISELY, C. & ROCKWELL, D. 1982 Self-sustained low-frequency components in an impinging shear layer. *J. Fluid Mech.* **116**, 157–186.

KOSEFF, J. R. & STREET, R. L. 1984a Visualization studies of a shear driven three-dimensional recirculating flow. *Trans. ASME: J. Fluids Engng* **106**, 21–29.

KOSEFF, J. R. & STREET, R. L. 1984b On endwall effects in a lid-driven cavity flow. *Trans. ASME: J. Fluids Engng* **106**, 385–389.

KOSEFF, J. R. & STREET, R. L. 1984c The lid-driven cavity flow: a synthesis of qualitative and quantitative observations. *Trans. ASME: J. Fluids Engng* **106**, 390–398.

MESEGUER-GARRIDO, F., DE VICENTE, J., VALERO, E. & THEOFILIS, V. 2011 Effect of aspect ratio on the three-dimensional global instability analysis of incompressible open cavity flows In *6th AIAA Theoretical Fluid Mechanics Conference*, Honolulu, Hawaii, vol. 3605. AIAA.

MESEGUER-GARRIDO, F., DE VICENTE, J., VALERO, E. & THEOFILIS, V. 2014 Three-dimensional global instability analysis of incompressible open cavity flows. *J. Fluid Mech.* (submitted).

MIGEON, C. 2002 Details on the start-up development of the Taylor–Görtler-like vortices inside a square-section lid-driven cavity for $1000 < Re < 3200$. *Exp. Fluids* **33**, 594–602.

MIGEON, C., PINEAU, G. & TEXIER, A. 2003 Three-dimensionality development inside standard parallelepipedic lid-driven cavities at $Re = 1000$. *J. Fluids Struct.* **17**, 717–738.

NEARY, M. D. & STEPHANOFF, K. D. 1987 Shear-layer-driven transition in a rectangular cavity. *Phys. Fluids* **30** (10), 2936–2946.

PARKER, K., VON ELLENRIEDER, K. D. & SORIA, J. 2007 Morphology of the forced oscillatory flow past a finite-span wing at low Reynolds number. *J. Fluid Mech.* **571**, 327–357.

PIOT, E., CASALIS, G., MULLER, F. & BAILLY, C. 2006 Investigation of the pse approach for subsonic and supersonic hot jets. detailed comparisons with LES and Linearized Euler Equation results. *Intl J. Aeroacoust.* **5** (4), 361–393.

POWELL, A. 1953 On edge tones and associated phenomena. *Acustica* **3**, 233–243.

ROCKWELL, D. 1977 Prediction of oscillation frequencies for unstable flow past cavities. *Trans. ASME: J. Fluids Engng* **99**, 294–300.

ROCKWELL, D. & KNISELY, C. 1980 Observations of the three dimensional nature of unstable flow past a cavity. *Phys. Fluids* **23**, 425–431.

ROCKWELL, D. & NAUDASCHER, E. 1979 Self-sustained oscillations of impinging free shear layers. *Annu. Rev. Fluid Mech.* **11**, 67–94.

ROSSITER, J. E. 1964 Wind-tunnel experiments on the flow over rectangular cavities at subsonic and transonic speeds. *Aeronaut. Res. Counc. R & M* 3438.

ROWLEY, C. W., COLONIUS, T. & BASU, A. J. 2002 On self-sustained oscillations in two-dimensional compressible flow over rectangular cavities. *J. Fluid Mech.* **455**, 315–346.

SHANKAR, P. N. & DESHPANDE, M. D. 2000 Fluid mechanics in the driven cavity. *Annu. Rev. Fluid Mech.* **32**, 93–136.

SORIA, J. 1996a An adaptative cross-correlation digital PIV technique for unsteady flow investigations. In *Proc. Australian Conf. on Laser Diagnostics in Fluid Mechanics and Combustion, Sydney, Australia* (ed. A. Masri & D. Honnery), vol. 1, pp. 29–48. University of Sydney, Sydney, Australia.

SORIA, J. 1996b An investigation of the near wake of a circular cylinder using a video-based digital cross-correlation particle image velocimetry technique. *Exp. Therm. Fluid Sci.* **12**, 221–233.

SORIA, J. 1998 Multigrid approach to cross-correlation digital PIV and HPIV analysis. In *13th Australasian Fluid Mechanics Conference, Melbourne, Australia*.

SORIA, J., CATER, J. & KOSTAS, J. 1999 High resolution multigrid cross-correlation digital PIV measurements of a turbulent starting jet using half frame image shift ®lm recording. *Opt. Laser Technol.* **31**, 3–12.

THEOFILIS, V. 2000 Globally unstable basic flows in open cavities. In *AIAA Paper* 2000-1965.

THEOFILIS, V. & COLONIUS, T. 2003 An algorithm for the recovery of 2- and 3-D BiGlobal instabilities of compressible flow over 2-d open cavities. *AIAA Paper* 2003-4143.

THEOFILIS, V. & COLONIUS, T. 2004 Three-dimensional instabilities of compressible flow over open cavities: direct solution of the biglobal eigenvalue problem. *AIAA Paper* 2004-2544.

THEOFILIS, V., COLONIUS, T. & SEIFERT, A. (ed.) 2001 Proceedings of the "AFOSR/EOARD/ERCOFTAC SIG-33 Global Flow Instability Control Symposium I", 23–25 September 2001, Creta Maris, Hersonissos, Greece.

DE VICENTE, J. 2010 Spectral multi-domain method for the global instability analysis of complex cavity flows. PhD thesis, Universidad Politécnica de Madrid.

DE VICENTE, J., PAREDES, P., VALERO, E. & THEOFILIS, V. 2011 Wave-like disturbances on the downstream wall of an open cavity In *6th AIAA Theoretical Fluid Mechanics Conference*, Honolulu, Hawaii, vol. 3754. AIAA.

DE VICENTE, J., RODRIGUEZ, D., THEOFILIS, V. & VALERO, E. 2010 Stability analysis in spanwise-periodic double-sided lid-driven cavity flows with complex cross-sectional profiles. *Comput. Fluids* **43** (1), 143–153.